Mesoscopic quantitative chemical analyses using STEM-EDX in current and next generation polycrystalline Ni-based superalloys

Kitaguchi, Hiroto; Jones, Ian; Chiu, Yu-Lung; Ding, Rengen; Hardy, Mark; Bowen, Paul

DOI:
10.1016/j.ultramic.2019.04.015

Document Version
Peer reviewed version

Citation for published version (Harvard):
Kitaguchi, H, Jones, I, Chiu, Y-L, Ding, R, Hardy, M & Bowen, P 2019, 'Mesoscopic quantitative chemical analyses using STEM-EDX in current and next generation polycrystalline Ni-based superalloys', *Ultramicroscopy*, vol. 204, pp. 55-72. https://doi.org/10.1016/j.ultramic.2019.04.015

Mesoscopic quantitative chemical analyses using STEM-EDX in current and next generation polycrystalline Ni-based superalloys

H.S. Kitaguchi[1*], Ian P. Jones[1], Yulung Chiu[1], Rengen Ding[1], Mark C. Hardy[2] Paul Bowen[1]

[1] School of Metallurgy and Materials, College of Engineering and Physical Science, The University of Birmingham, Edgbaston, Birmingham, B15 2TT, UK

[2] Rolls-Royce plc, PO Box 31, Derby, DE24 8BJ, UK

[*] Corresponding author. Tel.: +44 (0)121 414 5211, Fax: +44 (0)121 414 7468

h.kitaguchi@bham.ac.uk

Abstract

Quantitative chemical analyses of Ni_3Al based hardening precipitates (γ′) in polycrystalline Ni based superalloys have been conducted using energy dispersive X-ray spectroscopy (EDX), coupled with a scanning transmission electron microscope (STEM). The aim of the current investigation is 1) to evaluate the accuracy of calibration (k factor determinations and absorption corrections using a combination of differential X-ray absorption (DXA) and convergent beam electron diffraction (CBED)) by comparing with thermodynamic calculations and 2) to demonstrate the importance of the EDX chemical analysis by taking advantage of its unique capabilities to analyse sub-micron scale chemistries within a mesoscopic field of view under STEM. Our experimental findings show good agreement with the mole fraction ratio of γ′ to the disordered γ matrix predicted using the Lever rule on a thermodynamically stabilised unimodal superalloy, RR1000. The significance of analysing a statistically viable number of samples in thermodynamically metastable superalloys and the chemical fluctuations found in coarse γ′, sized above 200 nm on a scale of a few hundred nanometres in the context of solving a complex morphological evolution of γ′ particles is demonstrated.

Key words

Quantitative energy dispersive X-ray (EDX) Analysis; Differential X-ray absorption (DXA); Convergent beam electron diffraction (CBED); Superalloys; Gamma prime (γ′); Thermo-Calc Software

1. Introduction

Polycrystalline nickel-based superalloys, used for turbine discs with operating temperatures above 700˚C, are required to satisfy various physical and mechanical properties, from oxidation/corrosion resistance to monotonic tensile strength, creep and fatigue resistance [1, 2]. The superior mechanical properties are conferred by Ni_3Al based γ′ intermetallic hardening precipitates, which have an ordered $L1_2$ structure, perfectly coherent with the disordered γ face-centred cubic (fcc) matrix which is composed mainly of Ni, Co and Cr. The relentless drive for higher fuel efficiency and lighter gas turbine engines has resulted in the development of new generation Ni based superalloys which require an understanding of system thermodynamics in order to control elemental partitioning between the constituent phases [2-4]. A number of in-depth investigations of the partitioning between the two phases, i.e. γ′ and γ, have been carried out, focusing on site occupancies [5, 6], effect of solute elements [7] and, more recently, involving platinum group metal additions, such as Ta and W [3, 8]. The majority of the studies have been based on an atom probe tomography (APT) technique that is capable of detecting ions one-by-one from the tip of a needle-shaped sample by the application of either pulsed high voltage or pulsed laser and reconstructing the detected ions in three dimensions, conferring a superior detection limit and spatial resolution. However, the method has a limited analysis volume with typical dimensions of 100-150 nm in length and 50 nm in diameter that could make difficult data acquisitions from a whole phase/particle and could result in poor statistics when compositional variations between particles and phases are of interest [6]. Data analyses could potentially be complex, dependent on phases present in the sample and some specific elements of interest to quantify [9-12].

Studies of γ and γ′ element partitioning using energy dispersive X-ray (EDX) spectroscopy have been carried out, coupled with scanning transmission electron microscope (STEM) imaging [13-16]. Advantages of using the EDX-STEM technique are the efficiency of the data collection from a number of particles within a specimen and the wide range of sizes which can be analysed from the scale of nanometres to microns under in-situ microstructure

imaging using STEM. Nonetheless, analyses of a particle smaller than the TEM foil thickness, typically ~100 nm, can be an issue due to the influence of the surrounding matrix [17], often the case in γ and γ′ elemental partitioning studies. A few sample preparation techniques can be suggested to overcome the issue for γ′ chemical analyses. One is a filter clogging method [18] in which γ′ are extracted by dissolving the γ matrix electro-chemically [13]. The γ′ particles are subsequently captured using a micro-filter paper and are then analysed by TEM-EDX [15]. Another method is carbon extraction replicas [16, 19, 20] which involve an initial etch (removing some of the γ matrix), followed by coating the surface with a thin amorphous layer of carbon which is then detached from the surface along with the protruding γ′ particles by electro-chemical polishing underneath the carbon layer [20, 21].

An additional potential challenge with the EDX technique is preferential absorption of particular characteristic X-rays before the X-rays reach the EDX detector [22]. It is soft X-rays which are particularly absorbed by the sample, for example Al characteristic X-rays in a Ni matrix [13, 16, 23-28], hence it is necessary to carry out a careful calibration to correct for the absorption [16]. The calibration requires a supplementary experiment involving measurements of accurate sample thickness and density to define the effective mass travel distance inside the sample. The thickness measurement can be carried out using electron energy loss spectroscopy via a total-inelastic mean free path, with the zero-loss electron intensity as a reference, but the accuracy of the method is estimated to be ±20% [29]. Another method is convergent beam electron diffraction (CBED) [30, 31], which requires a number of time consuming steps, as detailed below; it is impractical to carry out the measurements for each EDX acquisition.

Some methods have been suggested for conducting the absorption correction without measuring the sample thickness. The ζ-factor method [23] is based on an absorption factor derived from the conditions of the analytical instruments, e.g. the detection efficiency and the electron acceleration voltage as well as beam current, that yield mass thickness, instead of studying separately the specimen thickness and density [23]. Morris et al. [32] first coined a method, later known as the differential X-ray absorption (DXA) method, in which two

characteristic X-rays from the same element: one absorption sensitive and the other insensitive are generated simultaneously in one spectrum, and used to correct for the absorption of light X-rays. Correction factors were derived by calculation after acquiring a number of spectra from various thickness regions and the effective mass path length determined by calculation from the ratio of the two characteristic X-rays. Quantitative analyses of a homogeneous Cu-Al binary system with a known stoichiometry were successfully demonstrated [32].

In the current investigation, quantitative chemical analyses of a current and a prototype next generation polycrystalline Ni based superalloy were conducted using a combination of the DXA and CBED techniques. The validity of the technique as well as elemental concentration variations between γ′ precipitates within a sample and within single γ′ precipitates were studied.

2. Material

The chemical compositions and thermal histories of each polycrystalline superalloy in the current study are shown in Tables 1 and 2, respectively. Three different grades of polycrystalline superalloy were studied with seven different variants, according to the thermal histories of super-solvus solution treatment and subsequent ageing. RRCoH is a next generation high Co content Ni superalloy that has undergone solution treatment only and was used for calibration purposes. RR1000 is a current generation superalloy which was solution treated and then given one of two isothermal ageing treatments; one at 900ºC and the second at 750ºC. RRAlH is a next generation superalloy with high Al content that was also subjected to the isothermal ageing described above. Each of the samples described above was subjected to a liquid nitrogen quench after super-solvus solution treatment. Another RRAlH sample was furnace cooled after solution treatment to create a bimodal γ′ distribution so as to compare the γ′ chemistries of the two different populations of γ′ within the sample after ageing at 850ºC. Additionally, pure Ni (>99.7%) flakes were used for calibration purposes.

3. Methodology: sample preparation and (S)TEM analysis

3.1. Wedge shaped TEM thin foil for calibration

In order for a precise calibration to measure the accurate thickness of the sample and the corresponding X-ray acquisitions at the region of interest, focused ion beam (FIB) was used to prepare a thin foil sample for the CBED analyses as well as for the measurements of NiKα (absorption insensitive) and NiLα (absorption sensitive) X-rays. An FEI Quanta 3D FIB-SEM was used to prepare the samples of RRCoH, RR1000 and pure Ni. In the final thinning stage, the ion beam was tilted relative to the sample width direction so that the sample became wedge shaped [33]. Figure 1 shows an SEM secondary electron micrograph of one of the thin foil wedges.

3.2. Thin foil sample for γ phase analysis

Twin-jet electro-polishing was used to prepare thin foil samples to analyse the γ chemistry. RR1000 after ageing at 750ºC for 150 hours was mechanically ground to 200 μm in thickness before being electrochemically polished in a twin-jet polishing apparatus using a 5% perchloric acid in methyl alcohol solution at -40ºC to produce TEM thin foil specimens that typically became 50-300 nm in thickness.

3.3. Carbon extraction replicas for γ′ analysis

For γ′ quantitative analyses, carbon extraction replicas were prepared in an attempt to eliminate the contribution of X-rays from the γ matrix. Subsequently to conventional mechanical polishing for metallographic sample preparations, each bulk sample was etched electro-chemically in a 10% orthophosphoric acid solution with de-ionised water at 2.5V for 5 seconds. The surface of the etched sample was covered by carbon by evaporating a pure carbon string using a Quorum Technologies Q150T EM Coater from a distance of 20 mm above the sample surface. Subsequently, the alloy underneath the carbon layer was polished electro-chemically using 20% perchloric acid in methyl alcohol so that the carbon layer with the γ′ precipitates was separated from the alloy surface. The detached carbon layer was thoroughly cleaned in de-ionised water before placing onto a 3 mm diameter mesh copper-grid for STEM observations and EDX acquisitions.

3.4. (S)TEM, CBED and EDX analysis

An FEI TECNAI F20 TEM was used for the TEM-CBED and (S)TEM-EDX analyses. For both the TEM and STEM, a 200 keV electron acceleration voltage was used. For the TEM-CBED analyses, the tilt angle towards the EDX detector: α tilt, was kept at 0º to measure the thickness of the region of interest. For the EDX acquisitions, an Oxford Instruments X-MAX 40 silicon drift detector coupled with Aztec Software, version 3.1 was used. The α tilt angle was set to 20° to increase the efficiency of X-ray acquisition. For the γ′ analyses, the whole particle was analysed in each measurement. Carbon and boron characteristic X-rays as well as Cu X-rays were generated from the TEM support grid. Pt can be detected from the protective layer applied during the FIB sample preparation and Ga can be detected from the ion beam. Those elements were selected as deconvolution elements that were included in the deconvolution process incorporated in the Aztec Software, but were eliminated from the quantification. Typical counting statistical errors of the major and minor elements are less than 5% and 10%, respectively, of the measured values. Standard deviations with 95% (2σ) confidence were calculated for the individual particles quantified. To determine the densities of the next generation superalloys, measurements using X-ray Diffractometry (XRD) were carried out to find the lattice parameters using a Philips X'Pert XRD, following studies carried out elsewhere [34].

4. Calibration

4.1. Absorption correction: Sample thickness determination and NiKα/NiLα EDX measurements

Convergent beam electron diffraction (CBED) patterns provide information on specimen thickness via the Kossel-Möllenstedt (K-M) fringes for a given *hkl* Bragg position [35] and the thickness at that position can be determined by measuring the fringe spacing corresponding to the angles ($\Delta\theta_i$) which are a function of the deviation from the Ewald sphere (s_i), the incident electron wave length (λ), the interplanar spacing (d) and the Bragg angle (θ_B) [35].

Regarding the relationship between EDX spectra and sample thickness, the equation below shows the relationship between the incident, i.e. generated X-ray intensity (I_0) and its intensity (I) attenuation by matter.

$$\boldsymbol{I = I_0 * exp\left\{-\left(\frac{\mu}{\rho}\right)\rho x\right\}} \quad \textbf{(Eq 1)}$$

where $\left(\frac{\mu}{\rho}\right)$ is the mass attenuation coefficient (MAC). ρ and x are the density and the path length of the generated X-ray inside the attenuator, respectively. With particular reference to this study, for the NiKα and NiLα X-rays that are present in each spectrum, the relationship above can be re-written by following the Goldstein treatment [22] of absorption in the thin film sample as below [32]:

$$\boldsymbol{\frac{I_{NiK}}{I_{NiK0}} = \tau_{NiK} * exp\left\{-\left(\frac{\mu}{\rho}\right)_{NiK} * \rho * \frac{1}{sin(\alpha+\theta)} * \frac{t}{2}\right\}} \quad \textbf{(Eq 2)}$$

$$\boldsymbol{\frac{I_{NiL}}{I_{NiL0}} = \tau_{NiL} * exp\left\{-\left(\frac{\mu}{\rho}\right)_{NiL} * \rho * \frac{1}{sin(\alpha+\theta)} * \frac{t}{2}\right\}} \quad \textbf{(Eq 3)}$$

I_{NiK0} and I_{NiL0} are the incident intensities of the Ni Kα and Ni Lα characteristic X-rays. I_{NiK} and I_{NiL} are the intensities of Ni Kα and Ni Lα measured by the EDX detector. α is the tilt angle of the sample toward the detector (20º in the current study) and θ is the take-off angle of the detector (11º). t and τ are the sample thickness and the detector efficiency, respectively. By combining Eq 2 and 3 and using natural logarithms,

$$\boldsymbol{ln\frac{I_{NiK}}{I_{NiL}} = \left[\left\{\left(\frac{\mu}{\rho}\right)_{NiL} - \left(\frac{\mu}{\rho}\right)_{NiK}\right\} * \rho * \frac{1}{sin(\alpha+\theta)} * \frac{1}{2}\right] * t + ln\frac{I_{NiK0}}{I_{NiL0}} + ln\frac{\tau_{NiK}}{\tau_{NiL}}} \quad \textbf{(Eq 4)}$$

Assuming $\left(\frac{\mu}{\rho}\right)_{NiL} \gg \left(\frac{\mu}{\rho}\right)_{NiK}$

$$\boldsymbol{ln\frac{I_{NiK}}{I_{NiL}} \approx \left[\left(\frac{\mu}{\rho}\right)_{NiL} * \rho * \frac{1}{sin(\alpha+\theta)} * \frac{1}{2}\right] * t + ln\frac{I_{NiK0}}{I_{NiL0}} + ln\frac{\tau_{NiK}}{\tau_{NiL}}} \quad \textbf{(Eq 5)}$$

Assuming the ratio of NiK_0 and NiL_0 is constant for a constant electron acceleration voltage, the natural logarithm of $\left(\frac{I_{NiK}}{I_{NiL}}\right)$ and the sample thickness t have a linear relationship within a homogeneous sample.

In the current study, the CBED technique and simultaneous acquisitions of the X-ray spectra were used for absorption calibrations using the liquid nitrogen quenched RRCoH and RR1000 wedge shaped samples which were regarded as single phase (γ) materials. The reason why the

two superalloys were chosen was to examine a potential difference in the results between the two materials due to their densities and/or MACs. CBED patterns were taken from various thickness regions and subsequently EDX spectra were acquired to determine the NiKα and NiLα ratio corresponding to each thickness measurement, as shown in the schematic diagram in Figure 2a. Examples of the CBED patterns and the corresponding EDX spectra can be found Figure 2b-e, taken from a thin and a thick region. In total, 19 and 14 individual thickness measurements and the corresponding EDX acquisitions were carried out using RRCoH and RR1000, respectively, as shown in Figure 3a. A straight line was drawn for each alloy, assuming $ln\frac{I_{NiK}}{I_{NiL}} \propto \boldsymbol{t}$, following Eq 4. The work flow introduced above, including the whole process of the EDX calibration, is illustrated in Figure 4; the work flow mentioned so far can be found in the middle column, down to the 4th row (shaded by yellow). First, it was noted that deviations of many of the data points from the straight lines were significant; this could be attributed to experimental uncertainties generated from the two independent measurements; the CBED was acquired using a CCD camera at the α tilt angle of 0º and EDX acquisitions was subsequently carried out at α=20º (Figure2a), which may have resulted in some experimental error. For example, in the EDX NiKα/NiLα determinations, the X-ray travel path could be different by tens of nanometres from the point of the CBED analyses, mainly dependent on the quality of the sample fabricated by the FIB technique. Nonetheless, the slopes for RRCoH and RR1000 were similar to each other, which suggested a similar MAC for NiLα ($MAC_{NiL\alpha}$) for the two superalloys. The slightly steeper slope for RRCoH than for RR1000 can be due to the slightly different densities which were determined to be 8.06 and 7.94 g/cm^3 for RRCoH and RR1000, respectively, using fcc γ lattice parameters determined for the two alloys measured by XRD, following studies elsewhere [36]. This led to the determination of the $MAC_{NiL\alpha}$ of 4.22*10$^{\wedge 3}$ cm^2/g for RRCoH and 4.08*10$^{\wedge 3}$ cm^2/g for RR1000 with a difference of less than 4%, although a strong dependence of MAC on absorber (sample) has been reported for various systems using EPMA [37-39], including a study of $MAC_{NiL\alpha}$ in a Ni-Si binary system [37]. In Ref. [37], it was reported that the $MAC_{NiL\alpha}$ in Ni_2Si decreased by approximately 20%, compared to that of pure Ni [37]. The studies above [37-39] were carried out using bulk samples in which

fluorescence of X-rays can significantly influence the emission of X-rays from a sample. This is negligible in the current study with thin foils up to 250 nm in thickness using two different types of superalloys having different Co contents. To examine the influence of Ni alloy chemistry on the $MAC_{NiL\alpha}$, a pure wedged Ni sample was prepared to measure the slope of Eq 4, as shown in Figure 3b with the circle data points and the fitted straight line. It was noted that the slope was less steep by 25% than for the superalloys. NiLα self-MAC has been studied by other researchers and values are included in Figure 3b. Henke et al and Heinrich [40, 41] derived the NiLα self-MAC in Ni from a MAC data base as $1.81*10^{\wedge 3}$ cm^2/g, as shown with the broken line in Figure 3b. That was very different from the result, $3.56*10^{\wedge 3}$ cm^2/g, using an analytical model and reported by Pouchou et al [42], shown with a dashed line in Figure 3b. The NiLα self-MAC in the current study resulted in $2.78*10^{\wedge 3}$ cm^2/g.

For the following sections, sample thicknesses were determined based on the straight line with the equation derived from the combined results of RRCoH and RR1000 by finding the ratio between NiKα and NiLα in each spectrum, as shown in Figure 3a. It should also be noted that it would be necessary to investigate $MAC_{NiL\alpha}$, separately, for other types of samples, e.g. austenitic steels. For thick samples, including Ni superalloys, then fluorescence will also become important.

4.2. Cliff-Lorimer k factor determination and EDX analyses with density determinations

The liquid nitrogen quenched RRCoH was used for Cliff-Lorimer k factor determinations for each metal element present in the alloys, except for the minor element: Hf which RRCoH does not contain, and for which theoretical values were applied. Kα characteristic X-ray counts were used for each element for the quantitative analysis, except for Hf, Ta and W, for which the Mα, the Mα and the Lα characteristic X-ray counts were used, respectively. In STEM mode, an EDX acquisition was carried out on as large an area as possible to cover a thickness region approximately between 50 and 150 nm, 10 μm^2 in area, on the RRCoH thin foil followed by a ratio calculation of NiLα to NiKα to determine the mean thickness of the region, and then to determine the Cliff-Lorimer k factors for the metal elements of interest, following the

relationship below:

$$\frac{C_A}{C_B} = \mu_B k_{AB} \frac{I_A}{I_B}, \quad \frac{C_A}{C_C} = \mu_C k_{AC} \frac{I_A}{I_C} \quad \ldots \quad \frac{C_A}{C_i} = \mu_i k_{Ai} \frac{I_A}{I_i}$$

$$C_A + C_B + C_C \ldots + C_i = 100\ \% \qquad \textbf{(Eq 6)}$$

where C_i , I_i and μ_i represent the weight percentages, the X-ray counts and the absorption correction factor for the *i* element which is dependent on the sample thickness and density in the current study. k_{Ai} represents the Cliff-Lorimer k factor of the *i* element relative to the A element which was designated the major element in each superalloy, here Ni. The k factors determined as well as the theoretical values can be found in Table 3 and the work flow so far for the current section can be found in the far right column in Figure 4.

In the actual particle/phase measurements of unknown chemistries, it is necessary to evaluate the influence of the density of each sample analysed, which may differ from that of RRCoH and RR1000. The slopes using RRCoH (8.06 g/cm^3) and RR1000 (7.94 g/cm^3) were concluded to be within error: the same as each other, which suggested the MAC was the same amongst the different grades of superalloy (Figure 3a), however the slope is actually a function of the density of the specimen. To be precise, that means that the MAC is regarded constant in the current study, but the absorption correction can be a variable dependent on the density of the sample. Therefore, density determinations for the unknown particle/phase analyses were carried out on the basis of the EDX results obtained. For the RR1000 γ′, unconstrained lattice parameter of 3.594 Å was taken from the literature, as measured by synchrotron X-ray diffractometer (XRD) [43]. The unconstrained γ′ lattice parameter in RRAlH was measured as 3.619 Å by XRD using carbon extraction replicas. In detail, for the first quantitative analysis, the density of RRCoH: 8.06 g/cm^3 and the straight line in Figure 3a (the combination of the RRCoH and RR1000 results) were used to determine a thickness and subsequently a composition. This composition was then used to calculate a new density. Dependent on the difference between the two densities, iteration was initiated by changing the slope of Figure 3a (see the work flow loop in the bottom left in Figure 4 for the illustrative explanations of the iteration.). In general, the difference of the densities between the γ of the quenched RRCoH and the γ′ in RR1000 and RRAlH was ± 5% which resulted in a difference of ~±0.3% for each

elemental concentration of absorption sensitive elements, e.g. Al. The reason why the alteration of the density becomes insignificant for the quantified value is because there are two opposite outcomes to be considered influencing the absorption correction factor on changing the density; one is the influence as a result of changing the slope and the other is the direct influence of density itself. For example, an increase of density leads to a steeper line of Figure 3a and therefore a smaller thickness corresponds to the measured Ni Kα/Lα ratio, i.e. increase of density results in decrease of thickness.

5. Applications

5.1. Quenched (unimodal) superalloy chemical analysis

5.1.1. γ′ chemical analysis

Figure 5 shows SEM and STEM micrographs on both RR1000 and RRAlH after the two different ageing treatments, either at 750ºC for 150 hours or at 900ºC for 1.5 hours. Liquid nitrogen quenching after solution treatment produced a unimodal γ′ distribution. Each sample showed either spherical or ellipsoidal γ′. The average sizes after ageing are similar to each other, although the ageing at 900ºC resulted in slightly coarser γ′: 70-80 nm in average diameter, compared to 50-60 nm after the lower ageing temperature of 750ºC for the two alloys. Table 4 shows γ′ chemistries against ageing temperatures for RR1000 and RRAlH. More than 25 individual γ′ particles were analysed for each variant and the average and the standard deviation were calculated. Thermo-Calc Software was used to calculate equilibrium chemical compositions at the two ageing temperatures using a database: TTNI8, provided by Thermotech Ltd., to compare with the results of the EDX experiments, assuming the γ′ nuclei grow and are stabilised at each ageing temperature. In Figure 6, filled and open data points show the EDX measurements and the Thermo-Calc predictions, respectively. Triangle and circle data points show the results for RR1000 and RRAlH, respectively. The two data of the same material from the two different ageing temperatures were connected each other by a solid (RR1000) or a broken line (RRAlH) to show the trend of the chemical composition with respect to the ageing temperature. Regarding the results for each alloying element shown in Figure 6a-j, trends in

the chemical concentrations for the two ageing temperatures measured by EDX and predicted by Thermo-Calc generally agree each other; for example as shown in Figure 6a, the Al concentrations for RR1000 γ′ decrease on increasing the ageing temperature, but plateau for RRAlH. With respect to the quantitative values, some are in good agreement with the thermodynamic predictions, such as Al in RR1000, but some elemental concentration differ, such as Co in RR1000. Co concentrations in γ′ were analysed in RR1000 by Chen et al [44] using STEM-EDX with various ageing durations at 800ºC. It was reported that Co can segregate at the core of the particle by measuring the centre of γ′ with an assumption of the particles morphology to be spherical and the thickness of the sample is equivalent to the diameter of the particle. The equilibrium Co concentration at 800ºC by analysing γ′ without Co segregations was concluded to be 6.8 at% [44]. The connecting line between the two EDX results, shown in Figure 6d (see the line connecting the solid triangles), predicts 7.1 at%Co at 800ºC, which agrees with Ref. [44] within the standard deviation of the current EDX results of ±0.37 at% for the 750ºC ageing. Comparable results were also reported using APT after ageing at 760ºC for between 8 and 16 hours using a trimodal [5] and a bimodal RR1000 [43]; Co concentrations of primary, secondary and tertiary γ′ were concluded to be between 6.07 and 6.68 at% for the three different generations of γ′ particles [5, 43].

General EDX measurements do not provide any insights regarding the site occupancies in an ordered structure, including the current study in the Ni_3Al based $L1_2$ structure. Nevertheless, some of the quantitative analysis in the current study showed correlations with theoretical calculations of the Ni_3Al site occupancy using Thermo-Calc as well as with other experimental analyses with a superior spatial resolution which allows direct observations of site occupancies. Bagot et al [5] analysed site occupancies of the alloying elements within γ′ in RR1000 by APT, by plotting each solute element relative to the position of the Ni atoms by aligning the analysis direction normal to the (001) plane. It was concluded that both Co and Cr preferred the Ni sub-lattice in the Ni_3Al based $L1_2$ structure [5]. Based on the conclusion above, Figure 6k shows a diagram for the sum of Ni, Co and Cr. It is noted that the total atomic fraction of the three elements is close to 75 at%: the theoretical atomic fraction of Ni in the Ni_3Al system.

Additionally, after combining Ni, Co and Cr, the difference between the EDX results and the Thermo-Calc predictions become smaller than for the Ni results alone (c.f. Figure 6j and k) and the difference after combining the three elements is within the standard deviation of the EDX results of Ni alone. For instance, for RR1000, the differences between the EDX results and the thermodynamic predictions for Ni were |1.02| and |1.67| at% at 750 and 900ºC, respectively (Figure 6j). Whereas, the values became |0.44| and |0.35| at% (Figure 6k) after combining the three elements, which difference are within the standard deviations of the Ni results, i.e. ±1.20 and ±0.99 at% at 750 and 900ºC (Figure 6j). The same approach is applied to the Al sub-lattice in the form of Al+Ti+Nb+Ta [1], as shown in Figure 6m, which also shows in general a better agreement between the EDX results and the thermodynamic predictions compared to the individual elements, particularly for RRAlH. This is mainly because of the results for Al and Nb; the Al EDX results were smaller than the Thermo-Calc predictions by approximately 9% and Nb showed the opposite by approximately 12%. The sum of the Al sub-lattice elements for RR1000 (Figure 6m triangles) showed the largest deviations between the EDX measurements and the thermodynamic predictions in Figure 6k-m that can be further studied in details.

Mo is believed to be a solid solution strengthening element in superalloys. In RR1000, Thermo-Calc predicted that only 8.3 % of the total Mo partitions to γ′ in the current temperature regime (Table 1 and Figure 6f): smaller than any other alloying elements in RR1000, e.g. Cr (9.7 – 12.7 % in γ′ between 750 and 900ºC). EDX results for Mo in RR1000 showed the largest deviations from the thermodynamic predictions of any alloying elements. The EDX results show that Mo is partitioning to γ′ more than 5 and 3 times than the thermodynamic predictions at 750 and 900ºC equilibrium, respectively (Figure 6f). Anomaly in Mo concentrations in γ′ has also been reported elsewhere for RR1000 [5, 43]. It is reported that Mo concentrations in intermediate sized γ′ (secondary γ′) (formed during the early stage of the cooling after the solution treatment at 1,120ºC) and fine sized γ′ (tertiary γ′) (formed at lower temperatures during the late stage of the cooling after solution treatment) resulted in 0.74 and 1.66 at%, respectively, in RR1000 aged at 760ºC for 16 hours [5]. The Mo quantitative results for the tertiary γ′ from Ref. [5] is within the standard deviation of the

current results after ageing at 750ºC for 150 hours. The site occupancy of Mo in γ′ was also studied by Bagot et al [5] who found that the majority of Mo occupied the Al sub-lattice in RR1000 [5]. Figure 7a shows predicted Mo site occupancies in γ′ using Thermo-Calc. 87 and 73% of Mo occupies the Al sub-lattice in γ′ equilibrium at 750 and 900ºC, respectively (Figure 7a). According to Thermo-Calc, 62 and 50% of Cr in γ′ occupy Al sub-lattice at 750 and 900ºC (Figure 7b), respectively. Taking account of the findings of the Mo and Cr site occupancy using Thermo-Calc, Figure 7c shows comparisons between the thermodynamic prediction and the EDX results of RR1000, including Mo and Cr; each fraction found in Thermo-Calc substituting Al was added by calculating using the corresponding fractions from the EDX results and the predictions. By considering the minor elements, i.e. Cr and Mo in Al sub-lattice, the difference between the Thermo-Calc predictions and the EDX results became significantly smaller (c.f. Figure 6m) that resulted in less than 0.5 at% in difference between the EDX and the predictions for both ageing at 750 and 900ºC.

5.1.2. γ chemical analysis and Lever rule using RR1000

Using thin foils of RR1000 aged at 750ºC for 150 hours, γ phase chemical analyses were conducted using the thin foils after twin-jet polishing. Quantitative results for γ can be found in Table 5 representing 20 individual γ spectra. Hf in γ was found to be below the detection limit, as found in other studies using APT [5]. In general, standard deviations from each quantified value in γ were higher than those from γ′ analyses, for example the standard deviations relative to the average values of Al and Ti in γ are approximately 4-5 times larger than those for γ′. Firstly, the results can be interpreted by the electron beam spot size applied in the two measurements; the beam was spread to the size of each γ′ to measure the whole region of the particle using the carbon extraction replicas, whereas the beam was converged for the γ measurements to avoid illumination of γ′ using the thin foil samples. Additionally, the inhomogeneity of the γ matrix dependent on the neighbouring microstructure due to differences of the interdiffusion coefficients of the alloying elements in γ′ and γ [44] can also be blamed for the large standard deviation on the γ analyses. Al and Ti depletion, as well as

enrichment of γ partitioning elements, e.g. Cr and Co, in γ adjacent to the γ′ particles have been reported elsewhere [44, 45].

Assuming the RR1000 is a binary system: γ and γ′, it is possible to study the ratio of the two phases present in the RR1000 by the Lever rule using the overall chemical composition and the EDX results of the γ and γ′ chemistry. An equation can be written as below, following a similar study carried out by Bagot et al. [5]:

$$\boldsymbol{C_{All} = \emptyset_{\gamma'} * C_{\gamma'} + \left(1 - \emptyset_{\gamma'}\right) * C_{\gamma}} \quad \textbf{(Eq 6)}$$

Where $\boldsymbol{C_{All}}$, $\boldsymbol{C_{\gamma'}}$ and $\boldsymbol{C_{\gamma}}$ are the concentrations in atomic percent of each alloy element in the material, γ′ and γ phases, respectively. In theory, a plot of $(\boldsymbol{C_{All} - C_{\gamma}})$ in y axis vs $(\boldsymbol{C_{\gamma'} - C_{\gamma}})$ in x axis yields a straight line with a gradient of $\boldsymbol{\emptyset_{\gamma'}}$: the γ′ mole fraction [5]. Using one of the EDX γ phase measurements, the nominal composition of RR1000 (Table 1) and the γ′ average chemistry from the EDX results (Table 4), a mole fraction of γ′ and a regression error from the fitted straight line were determined. After 20 measurements of the γ phase, an average of the γ′ phase fraction and an average of regression error together with the standard deviations were calculated and shown in the right hand side of Table 5 and three representative results from the smallest γ′ fraction (44.1 mol%), intermediate fraction (45.7 mol%) and the largest fraction (47.3 mol%), yielded by Eq 6, are shown in Figure 8. It was found that a γ′ mole fraction of 45.6 ± 2.2 at%, where the Thermo-Calc results showed 45.1 at% at 750ºC equilibrium. It should be noted an excellent R squared regression value of 0.9971 ± 0.0043 which can be attributed to the sample used in the current study; it was thermodynamically stabilised by the 150 hour ageing to which temperature all the γ′ corresponded, unlike studies using a ternary component found in other studies [46]. It is also noted that the percentage of the standard deviation of the average γ′ fraction is close to 5.0%, which is significantly higher than that of the R squared regression value of less than 0.5%. The results suggest that each EDX analysis of γ and the average values of γ′ applied in the current task showed good agreement with each other to yield each γ′/γ ratio: a successful calibration process achieved in the current study. On the contrary, the calculated γ/γ′ ratios from each EDX γ phase measurement showed a large deviations which can be caused by the

chemical inhomogeneity in the γ matrix, as mentioned earlier. The EDX results of the γ composition was fluctuated depending on the electron trajectory through the thin foil, which was typically 40-100 nm in thickness; the more the electrons travelled through γ adjacent to γ′ where the γ former enriched and γ′ former depleted, the more the γ′ fraction yielded, and vice versa.

5.2. Furnace cooled (bimodal) γ′ chemical analysis using RRAlH

5.2.1. Fine and coarse γ′ chemical analysis

Superalloys can contain different generations of γ′ with different sizes and morphologies within a material, when solution treatments are carried out below the γ′ solvus and/or cooled slowly after the heat treatment [45]. It is claimed that changing the degree of diffusion and the supersaturation of γ′ formers during cooling after solution treatment can create different generations of γ′ [45, 47]. Figure 9 shows SEM micrographs of RRAlH furnace cooled after solution treatment and subsequently aged at 850ºC for 4 hours. The resultant microstructure shows a bimodal γ′ distribution containing coarse cuboidal γ′ approximately 200 – 500 nm across and fine spherical γ′ less than 100 nm in diameter, as identified by two circles in Figure 9a. Figure 10 and Table 6 show a summary of the γ′ chemistry of fine γ′ (Fγ′) and coarse γ′ (Cγ′) with measurements of 38 and 58 individual particles, respectively. Regarding Figure 10, open data points and filled data points show the results of individual measurements and the average along with its standard deviation, respectively. As mentioned earlier, it is important to measure the thickness of each sample in EDX quantitative analyses. Particularly for the Cγ′, morphologies of the particles were complex which made it difficult to predict the thickness of each Cγ′ from micrographs. However, the indirect measurement of the average thicknesses of particles from the NiKα/NiLα ratios enabled analyses of particles with various morphologies.

It is noted from Table 6 that the standard deviations of each alloying element in Fγ′ are larger than those in Cγ′, despite the counting statistical errors of each measurement being comparable. It is also noted from Table 6 for Fγ′ that, by summing Ni, Co and Cr, the

percentage of the standard deviation of the sum of the three major elements, i.e. Ni, Co and Cr, is 1.50 %, that is smaller than any of the three individual errors of Ni (2.56%), Co (7.59%) or Cr (44.1%). Unlike for RR1000, Thermo-Calc predicted approximately 70% of Cr atoms occupy in the Ni sub-lattice between 600 and 900ºC in the RRAlH system. Figure 11a shows the relationship between Ni and Cr concentration in individual Fγ′ particles that shows a strong trend for a decrease of the Ni concentration with increase in Cr. This can indicate that Cr substitutes strongly for Ni in the Ni sub-lattice in the RRAlH system, in agreement with the thermodynamic predictions. Comparable trends were found for alloying elements known to substitute for Al [1], as shown in Figure 11b-c. There is a relationship between Al and either Nb or W such that Al concentration decreases on increasing the amount of Nb or W in Fγ′. Interdiffusion coefficients amongst the alloying elements in γ′ in superalloys can be categorised into two groups. One is the major elements of Ni and Al as well as Co that have 10^{-13} – 10^{-19} m^2/s interdiffusion coefficient between the precipitation and ageing temperature: 1,100 and 700ºC [13, 48, 49]. Other transition metal elements, including Cr and Nb, have distinctively smaller diffusion coefficients by a factor of more than two orders of magnitude at the ageing temperature of 850ºC [49-51]. W was reported to have an activation energy similar to or higher than that of Nb [52], hence W can be categorised in the group of Cr and Nb. Fγ′ precipitates after the Cγ′ was generated during furnace cooling after solution treatment. Other studies report that fine γ′ less than 100 nm in diameter in the as-solution treated condition showed significant chemical variations in bimodal γ′ RR1000 after a controlled cooling below 0.16ºC/s [13, 17]. This could possibly be caused by chemical inhomogeneity in the neighbourhood of γ′, formed prior to the fine γ′, in particular for the solid solution and major γ′ constituent elements, e.g. Cr and Al. In the current study, many Fγ′ were predicted to have non-equilibrium chemical compositions at the start of the ageing at 850ºC dependent on the timing of the precipitation and/or the chemical inhomogeneity of the γ phase due to pre-formed Cγ′. During ageing for 4 hours, Co can diffuse approximately 85 nm [44], comparable to the radius of Fγ′, or further. However, the elements, categorised as the latter group, i.e. Cr, Nb and Cr, can only diffuse one order of magnitude less or shorter.

This is less than many of the Fγ′ radii. It is suggested in the current study for the slow diffusion solute elements, i.e. Cr, Nb and W, that the EDX results for Fγ′ showed large standard deviations due to the insufficient time given to achieve a thermodynamically stable condition.

5.2.2. Concentration profile within coarse γ′

Cγ′ coarsens to cubic and eventually complex morphologies that often show gaps running toward the centre of a Cγ′ from the face of the particle, as indicated by the arrows in Figure 9a. There has been much research on the formation of the unique morphology of γ′. Some have suggested it was a consequence of splitting of a cubic γ′ that was energetically favourable involving an interplay between the interfacial energy and the elastic strain energy inside the γ′ [44, 53]. Some suggested the splitting morphologies could be replicated by a coalescence process taking account of four anti-phase domains in the $L1_2$ ordered γ′ particles [54]. Figure 12a shows a STEM dark field micrograph of Cγ′ in the course of morphological evolution, as delineated by a square. It can be seen there are four connected cubic γ′ particles lying diagonally, sized approximately 200 nm with a narrow gap of width and depth 10 and 50 nm, respectively. Concentration profiles were studied, as delineated by the rectangle with an arrow indicating the analysis direction in Figure 12a. It is apparent in the dark field image that the region of interest (ROI) has various thicknesses as shown quantitatively in Figure 12b with triangle data points measured by the NiKα/NiLα method. To demonstrate the impact of the thickness determination, Figure 12b also shows the results of Al and Ni assuming a uniform thickness across the ROI of 100 nm with open circles and squares together with the quantitative results of Al and Ni concentrations corrected by the measured thickness with filled circles and squares. It is apparent that the Al concentration profile does not show a clear trend on assuming a constant thickness (open circles). Conversely, a depletion of Al from 14.0 at% in the cube γ′ region to 12.8 at% at 200 nm in distance is apparent after the correction of the thickness (filled circles). To a lesser extent, the symmetry of the Ni profile relative to the depletion at 200 nm in distance became clearer by plotting with the corrected thicknesses (filled squares). The

narrow gap in the Cγ′ is believed to be the region where splitting/coalescence of the Cγ′ particle has occurred. According to Thermo-Calc, 70% of the Mo in γ′ partitions to the Al sub-lattice at 850ºC. Considering also the Cr partitioning calculated by the Thermo-Calc, as mentioned above, the composition of the region at 200 nm is calculated as $(Ni_{0.82}Co_{0.14}Cr_{0.03}Mo_{0.01})_{2.48}(Al_{0.44}Nb_{0.39}Ta_{0.06}W_{0.05}Cr_{0.04}Mo_{0.02})_{1.00}$. More than half of the Al sub-lattice turned out to be occupied by elements other than Al, mainly by Nb (nearly 40 at%). The theoretical stoichiometric ratio of Ni to Al sub-lattice is 3:1, but was resulted in 2.48:1.00. In other studies on RR1000, it was concluded to be 3.3:1.0 [5] and 2.6:1.0 [13] for the tertiary and secondary γ′ formed during cooling after solution treatment and stabilisation by isothermal ageing. The current study showed a larger deviation than other studies which could be explained by active diffusion in the particular region examined. For example, Al is reported to diffuse via the Ni sub-lattice which is a distinctive diffusion mechanism for Al [50, 55].

W was quantified using Lα counts instead of Mα, because Ta Mα (a γ′ forming element in superalloys) overlaps significantly. However, the W Lα peak at 8.40 eV also overlaps with the major element Ni Kβ (8.26 eV). It is noted that the W concentration rose to more than 1.5 at% at 200 nm. This could be further investigated using other nano-chemical spectroscopies, e.g. ATP, without deconvolution processes or capable of acquisitions of better noise to peak ratios, to confirm the current data. Each element showed either a single trough or peak across the ROI, except for Cr which also showed two troughs either side of the peak at 140 and 240 nm. Other studies reported a significant difference in the Cr interdiffusion coefficient between γ and γ′ [13]. This could be an indication of a unique flux and/or the rate of Cr crossing the ROI. The cause of the concentration fluctuation is currently under investigation.

6. Conclusions

Mesoscopic scale: from tens to hundreds of nanometres, quantitative chemical analyses using STEM-EDX were conducted and the accuracy of the quantitative results and the significance of the technique applied were investigated using a current and a next generation polycrystalline Ni based superalloy. The main findings are summarised as below:

1. Using a thermodynamically stabilised unimodal RR1000 and a combination of the DXA and CBED methods, as a part of X-ray absorption calibrations, successful quantification of unknown samples was achieved for the two phases in the component: γ′ and γ, which was validated via the Lever rule;
2. In particular in bimodal γ′, particularly for Fγ′ which precipitated at a later stage of the cooling after the solution treatment, standard deviations can be as large as 45% of the quantified value, e.g. Cr: 2.90±1.28 at% in Fγ′ in RRAlH, after ageing at 850ºC for 4 hours, and measurements of more than 30 individual particles. This was suggested to be due to a slow diffusion rate for certain alloying elements and the lack of time provided for the system to equilibrate;
3. EDX results for individual elements in γ′ often showed deviations from thermodynamic predictions using Thermo-Calc Software. However, the results for the total content of either the Al or Ni sub-lattices within the $L1_2$ ordered structure, summing each element predicted by Thermo-Calc, were in good agreement with each other, with a typical error of a few percent of the quantified values using unimodal RR1000 and RRAlH;
4. After studying two grades of superalloys: RR1000 and RRAlH, it is suggested that partitioning of Mo and Cr can alter either the Al or Ni sub-lattice by changing overall the system (chemistry) of the material. Mo substitutes preferentially for Al in RR1000. Cr can substitute preferentially for Al below 900ºC in RR1000, but substitutes preferentially for Ni in Fγ′ in RRAlH.
5. Indirect measurements of sample thickness using the combination of the DXA and CBED methods can be a powerful tool to quantify concentration profiles of absorption sensitive elements, e.g. Al in Ni, across geometrically ununiformed regions. X-rays of minor element overlapping with a peak of a major element may need to be carefully assessed to confirm the accuracy of quantitative values in the current study. Complementary studies to validate the current results are currently sought using a technique with a superior noise to peak ratio without peak deconvolution processes required.

Acknowledgement

The joint support of the UK Engineering and Physical Sciences Research Council (EPSRC) and Rolls-Royce plc. under the Strategic Partnership is gratefully acknowledged. HK is grateful for generous considerations from Rolls-Royce Plc. for the supplement of samples and the permission for the publishing data. HK also thanks to the fruitful discussions of the EDX calibrations with Drs James Sagar and Pinard Philippe from Oxford Instruments.

Table 1 Actual chemical compositions of RRCoH and RRAlH and the nominal composition of RR1000

Alloy ID		B	C	Al	Ti	Cr	Co	Nb	Mo	Hf	Ta	W	Ni
RRCoH	wt%	0.03	0.03	2.9	4.0	13.8	23.6	1.5	3.0	0.0	3.9	1.7	45.5
	at%	**0.16**	**0.15**	**6.2**	**4.9**	**15.5**	**23.4**	**1.0**	**1.8**		**1.2**	**0.6**	**45.1**
RR1000	wt%	0.02	0.03	3.0	3.6	15.0	18.5	0.0	5.0	0.5	2.0	0.0	52.4
	at%	**0.08**	**0.13**	**6.4**	**4.3**	**16.5**	**17.9**		**3.0**	**0.2**	**0.6**		**51.0**
RRAlH	wt%	0.03	0.02	4.1	0.0	11.8	17.8	7.9	2.3	0.0	3.0	2.5	50.5
	at%	**0.14**	**0.10**	**9.0**		**13.4**	**17.8**	**5.0**	**1.4**		**1.0**	**0.8**	**51.5**

Table 2 Summary of thermal histories of the three superalloys

Alloy ID	Solution Heat treatment (Liquid nitrogen quench unless otherwise stated) Temperature (^{o}C) / Time (hours)	Ageing Heat treatment
RRCoH	1,185 / 1.0	---
RR1000	1,160 / 1.0	---
		900 / 1.5
		750 / 150
RRAlH	1,175 / 1.0	900 / 1.5
		750 / 150
	1,175 / 1.0 + Furnace Cooling	850 / 4.0

Table 3 Summary of measured k factors using RRCoH and the theoretical values [35]

Element		Ni	Al	Ti	Cr	Co	Nb	Mo	Hf	Ta	W
Applied X-ray line		Kα	Kα	Kα	Kα	Kα	Kα	Kα	Mα	Mα	Lα
Energy [keV]		7.480	1.486	4.512	5.415	6.931	16.615	17.480	1.646	1.712	8.398
k factor	Measured	**---**	**0.563**	**0.854**	**0.901**	**1.006**	**6.071**	**6.460**	**---**	**1.200**	**1.881**
	Theoretical	1.000	0.793	0.843	0.883	0.995	4.743	5.712	1.214	1.222	1.960

Table 4 Summary of γ′ chemistries of the sample quenched after iso-thermal ageing. (STD: standard deviation, shown in ± at%)

Alloy ID	Ageing [°C/hours]		Al	Ti	Cr	Co	Ni	Nb	Mo	Hf	Ta	W
RR1000	750/150	Average	11.91	9.22	2.20	6.57	67.43	---	1.35	0.27	1.07	---
		STD	0.67	0.65	0.60	0.37	1.20		0.31	0.13	0.20	
	900/1.5	Average	11.39	9.45	2.55	8.35	65.92		1.01	0.27	1.06	
		STD	0.68	0.30	0.40	0.29	0.99		0.15	0.07	0.12	
RRAlH	750/150	Average	12.98	---	1.68	9.75	63.81	9.17	0.44	---	1.38	0.83
		STD	0.87		0.53	1.08	1.17	0.84	0.24		0.23	0.14
	900/1.5	Average	12.88		2.87	12.33	60.50	8.79	0.50		1.37	0.75
		STD	0.90		0.32	1.10	1.57	0.98	0.16		0.26	0.19

Table 5 Summary of γ matrix chemistry of RR1000 after 750ºC for 150 hours and γ′ mole fraction analyses (STD: standard deviation, calculated using the specified number of the samples, mentioned in the text.)

Alloy ID and ageing condition		Gamma Phase Chemical Analysis Results								Lever rule results	
		Al	Ti	Cr	Co	Ni	Mo	Hf	Ta	γ′ mole fraction [%]	R Square
RR1000 (750°C for 150 hours)	Average	1.64	0.85	29.26	25.94	37.38	4.84	0.00	0.06	45.6	0.9971
	STD	0.47	0.25	2.06	1.13	1.56	0.80	---	0.06	2.2	0.0043

Table 6 Summary of fine and coarse γ′ chemistry of RRAlH after 850ºC for 4 hours, followed by furance cooling. (STD: standard deviation, shown in ± at%)

		Al	Cr	Co	Ni	Nb	Mo	Ta	W	Cr+Co+Ni
Fine γ′ (Fγ′)	Average	12.73	2.90	9.04	63.00	9.46	0.70	1.03	1.14	74.92
	STD	1.04	1.28	0.69	1.61	1.07	0.34	0.17	0.31	1.12
Coarse γ′ (Cγ′)	Average	13.81	2.63	11.01	62.24	7.70	0.51	1.34	0.77	75.80
	STD	1.02	0.41	0.44	1.10	0.56	0.23	0.16	0.19	1.06

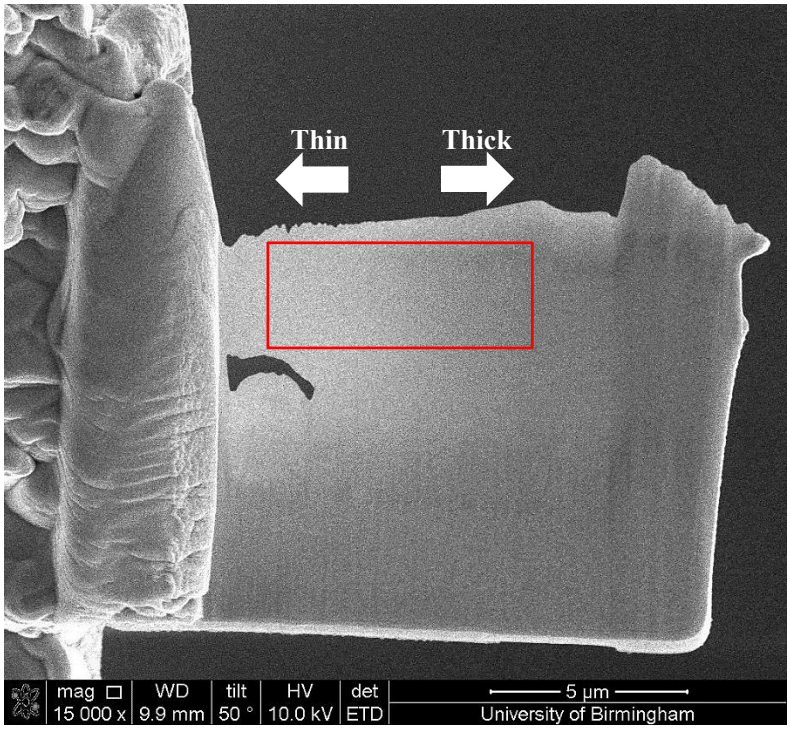

Figure 1 SEM secondary electron micrograph of a TEM thin foil wedge sample. The rectangle shows the area used for the calibration (See Section 4.1) from thin (left) to thick (right).

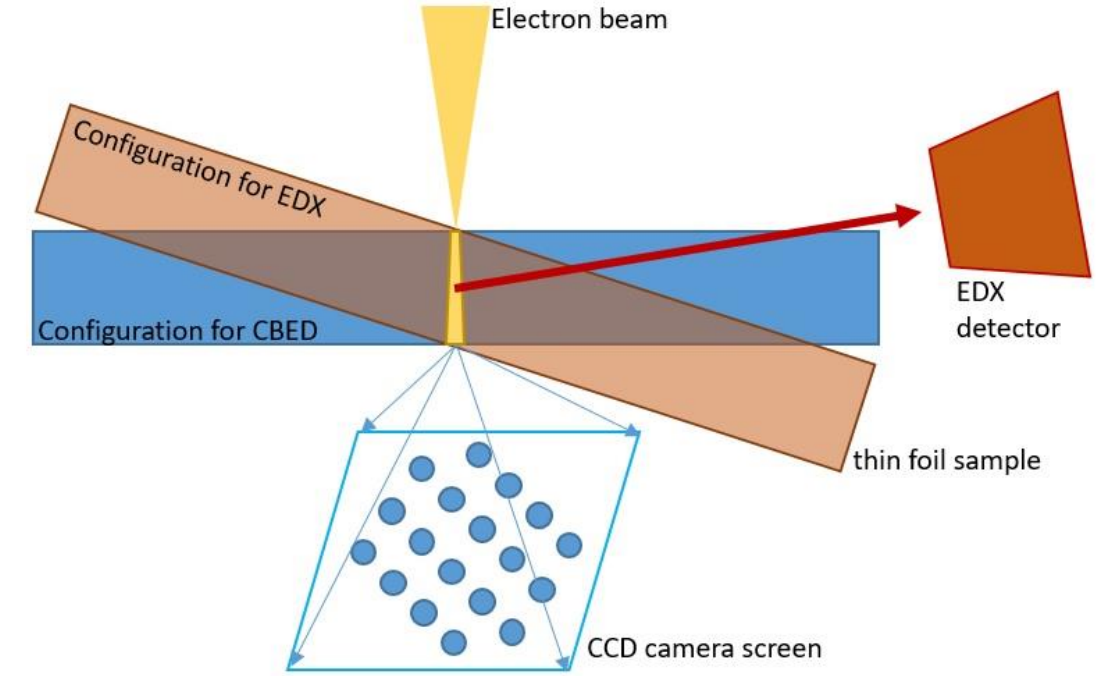

(a)

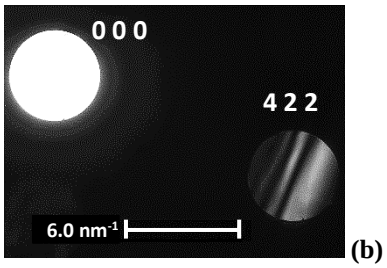

(b)

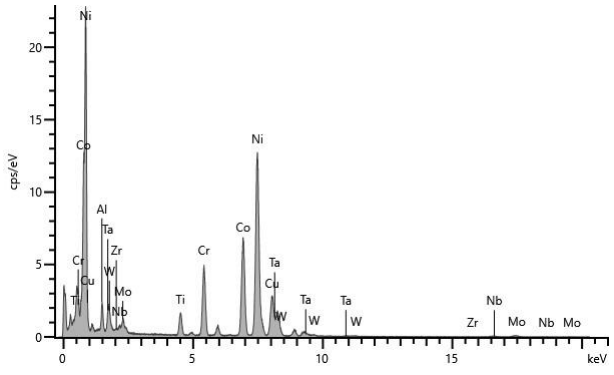

(d)

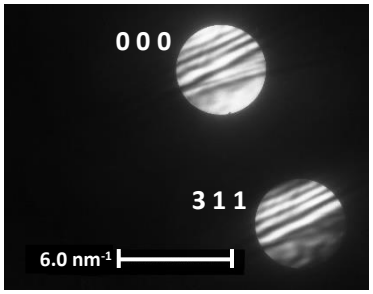

(c)

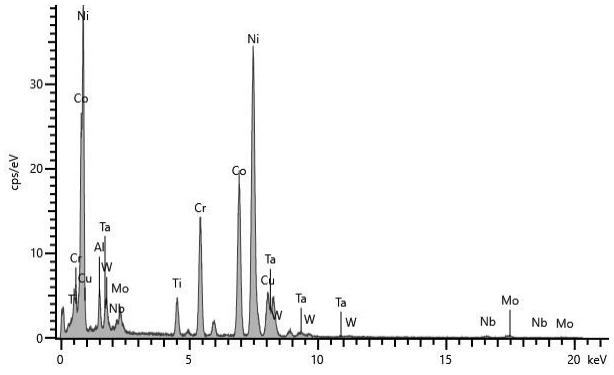

(e)

Figure 2 Schematic (2 dimensional) diagram of the two measurements of CBED and EDX, assuming the thin foil fabrication was perfectly carried out by the FIB sample preparation (a). Examples of the experimental results of the CBED patterns (b-c) and the corresponding EDX spectra (d-e) from two individual regions: a thin and thick region in (c, d) and (c, e), respectively.

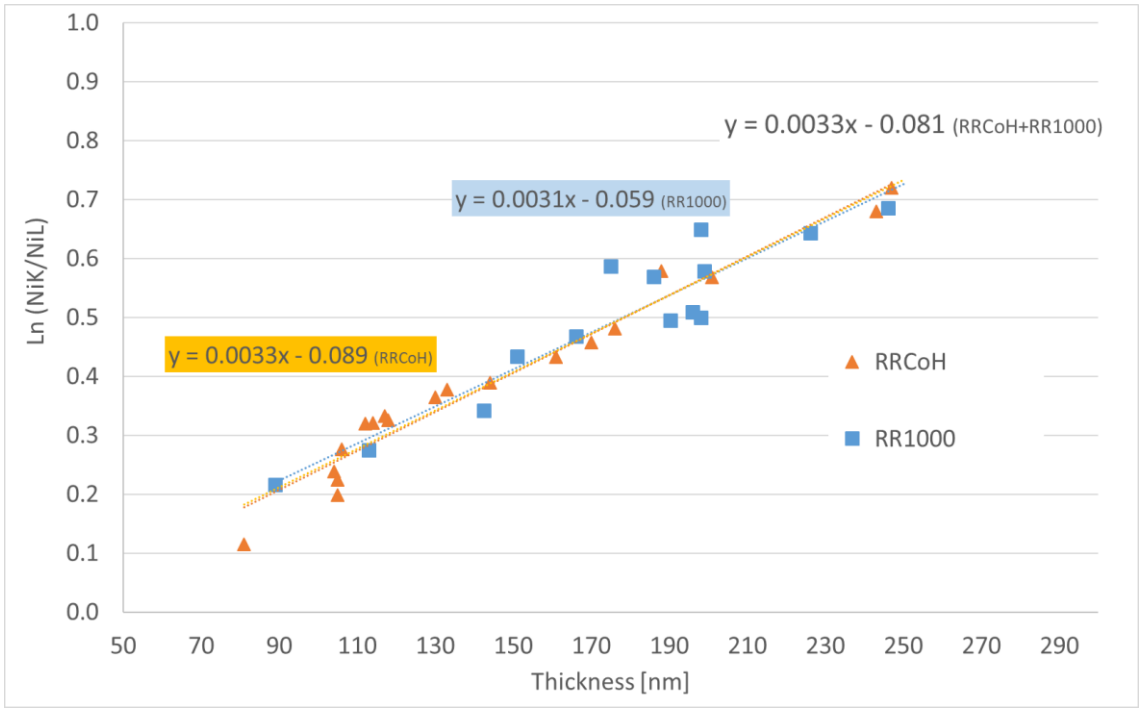

a)

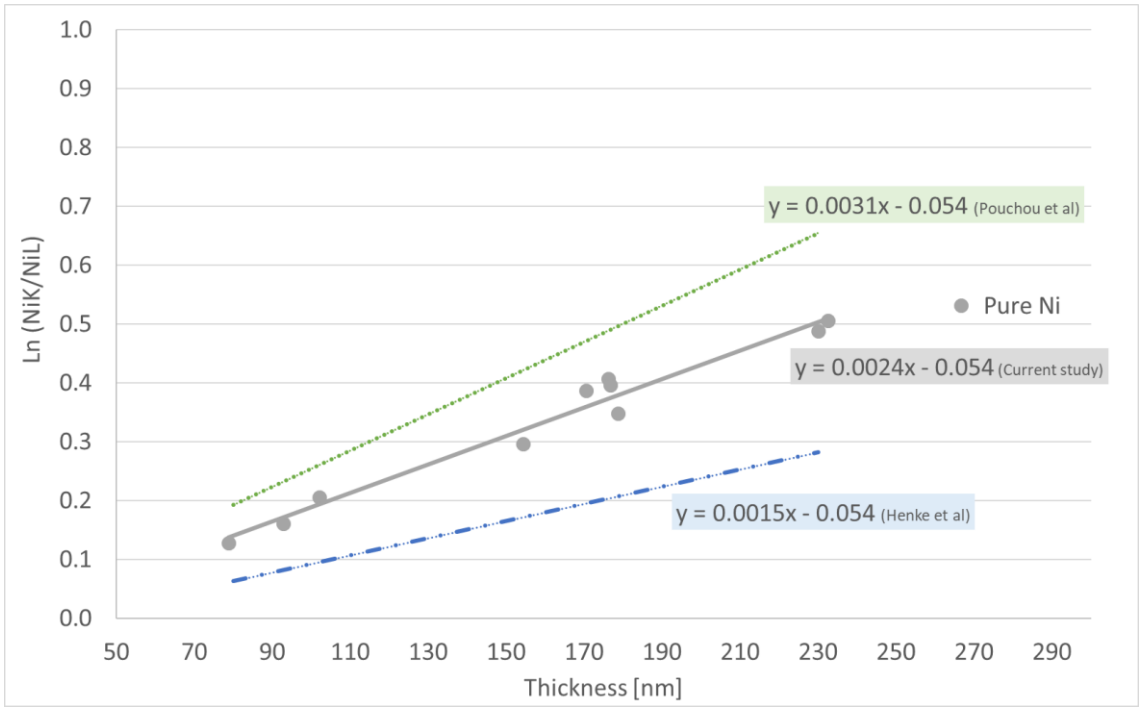

b)

Figure 3 Thickness of the thin foil against natural logarithm of NiKα/NiLα after acquisitions of EDX spectra as well as corresponding CBED fringes. (a) Results from quenched RRCoH and RR1000 and (b) results from pure Ni measured (circle data points and the fitted solid line) compared with the broken line derived from the $MAC_{NiL\alpha}$ of Ref. [40, 41] and the dashed line derived from the $MAC_{NiL\alpha}$ of Pouchou et al [42].

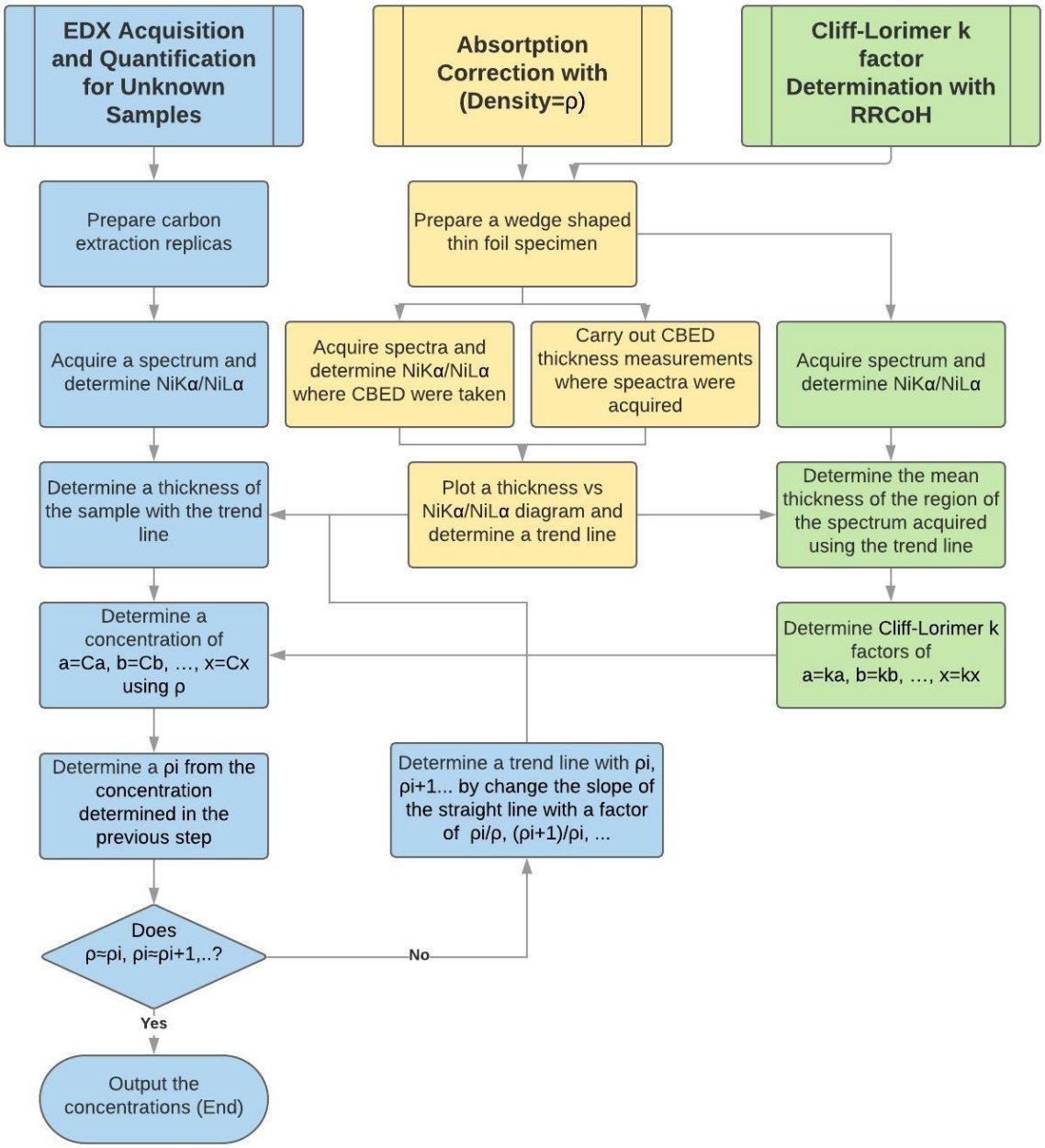

Figure 4 Calibration process flow chart; illustrating the absorption corrections in the middle column, the Cliff-Lorimer k factor determinations on the right and the unknown sample spectrum acquisitions and quantification on the left hand side.

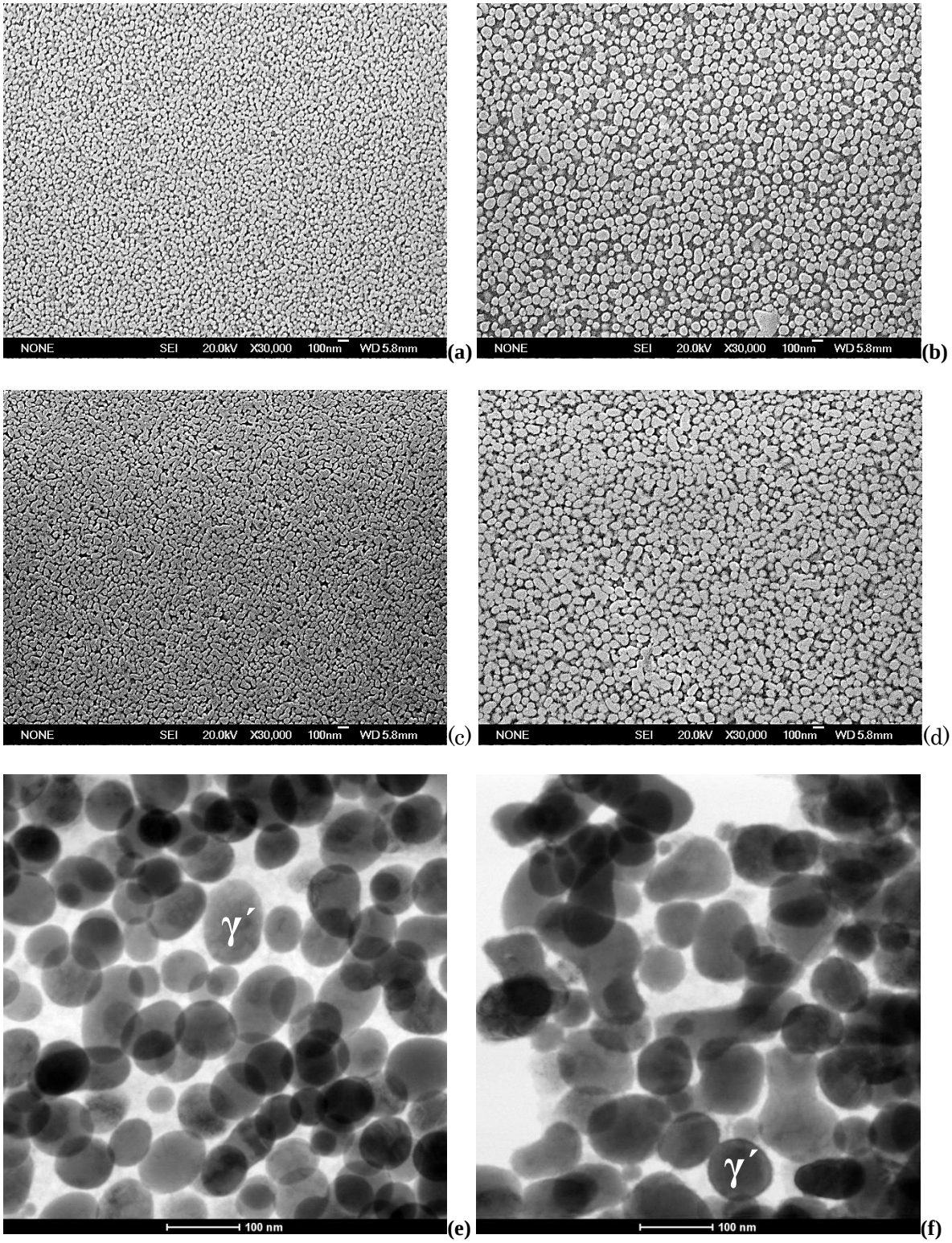

Figure 5 SEM secondary electron micrographs of the quenched and aged samples and representative STEM bright field micrographs of carbon extraction replicas with a higher magnification

- **(a) SEM RR1000 after 750ºC ageing**
- **(b) SEM RR1000 after 900ºC ageing**
- **(c) SEM RRAlH after 750ºC ageing**
- **(d) SEM RRAlH after 900ºC ageing**
- **(e) STEM RR1000 after 900ºC ageing**
- **(f) STEM RRAlH after 900ºC ageing**

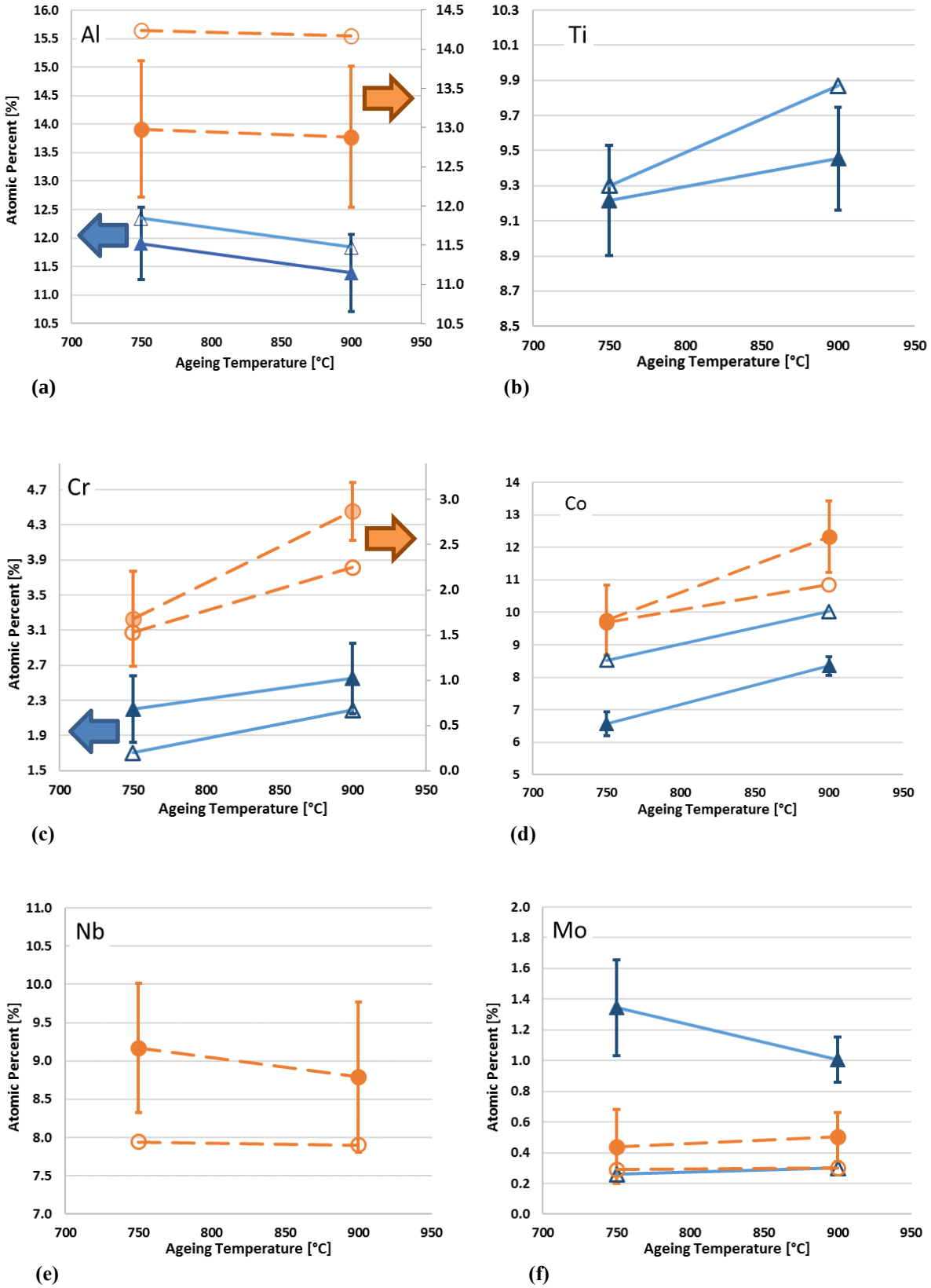

Figure 6 Summary of γ´ chemical analyses using quenched samples after ageing at 750 and 900ºC showing the difference between the ageing temperatures and thermodynamic calculations by Thermo-Calc Software. The filled and open triangles denote the EDX and the Thermo-Calc results for RR1000 (blue), respectively. The filled and open circles denote the EDX and the Thermo-Calc results for RRAlH (orange), respectively. Note some of the results with double Y axis with indictions with arrows.

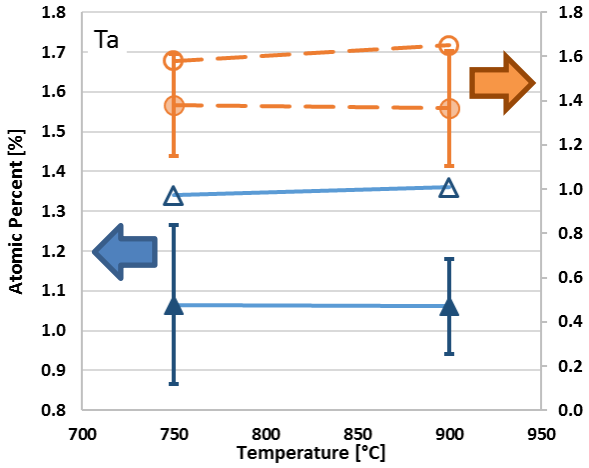

(g)

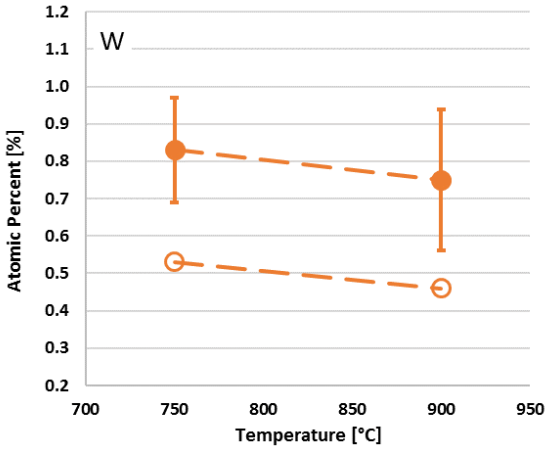

(h)

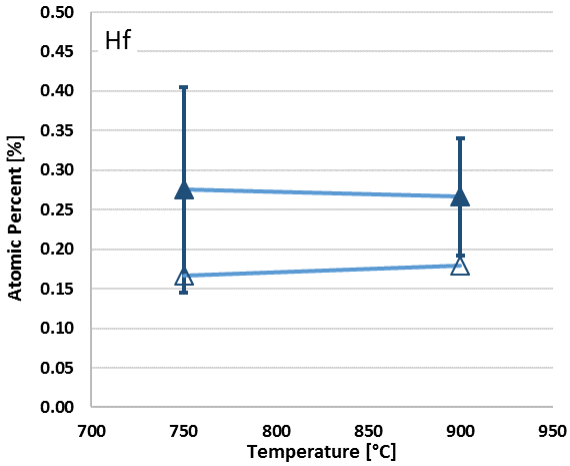

(i)

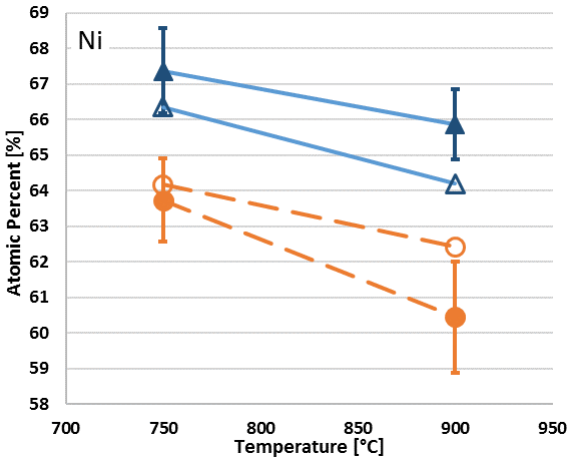

(j)

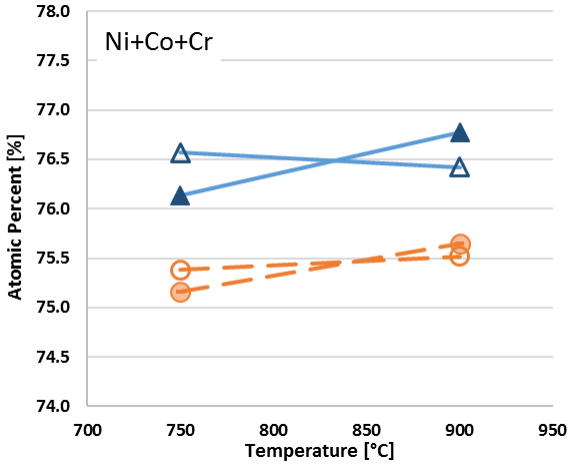

(k)

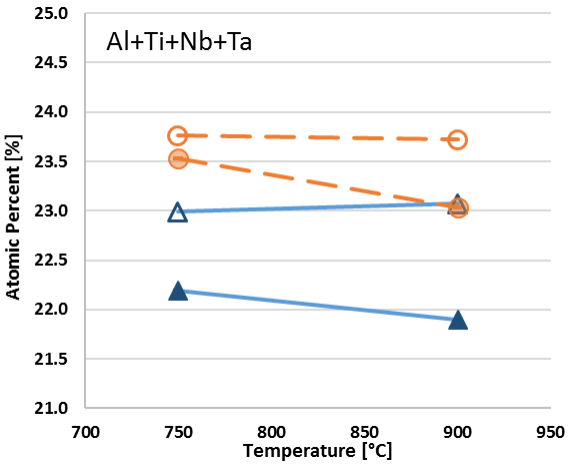

(m)

Figure 6 (Continued)

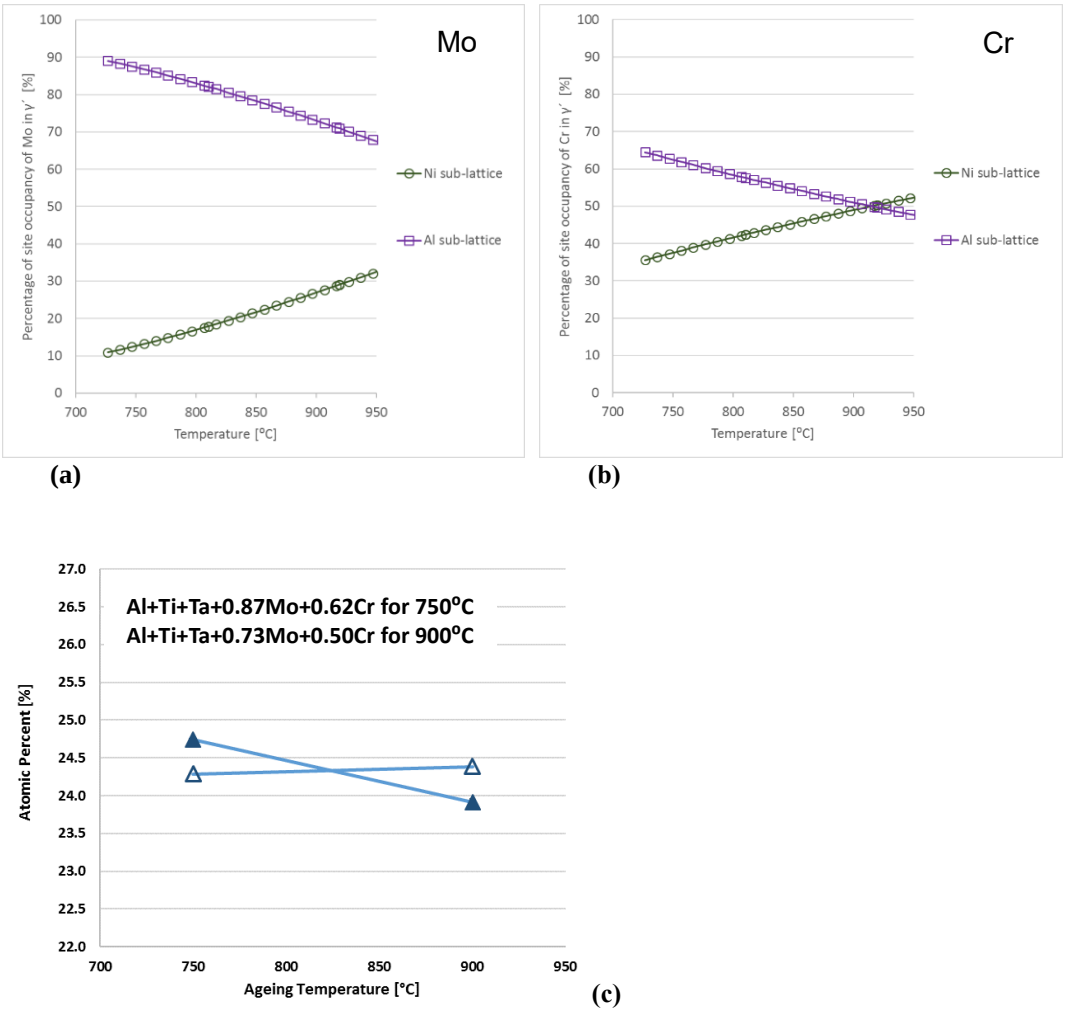

Figure 7 Site occupancies for Ni sub-lattice and Al sub-lattice in γ´ in RR1000, calculated by Thermo-Calc Software under TTNI8 for Mo (a) and Cr (b). Using the results of (a) and (b), elements for Al sub-lattice: Al, Ti, Ta, Mo and Cr in γ´ in RR1000 were re-calculated in (c) to demonstrate better agreement with thermodynamic predictions, compared to those without consideration of Mo and Cr (c.f. Figure 6m). Open data points are from Thermo-Calc Software and filled data points are based on EDX results.

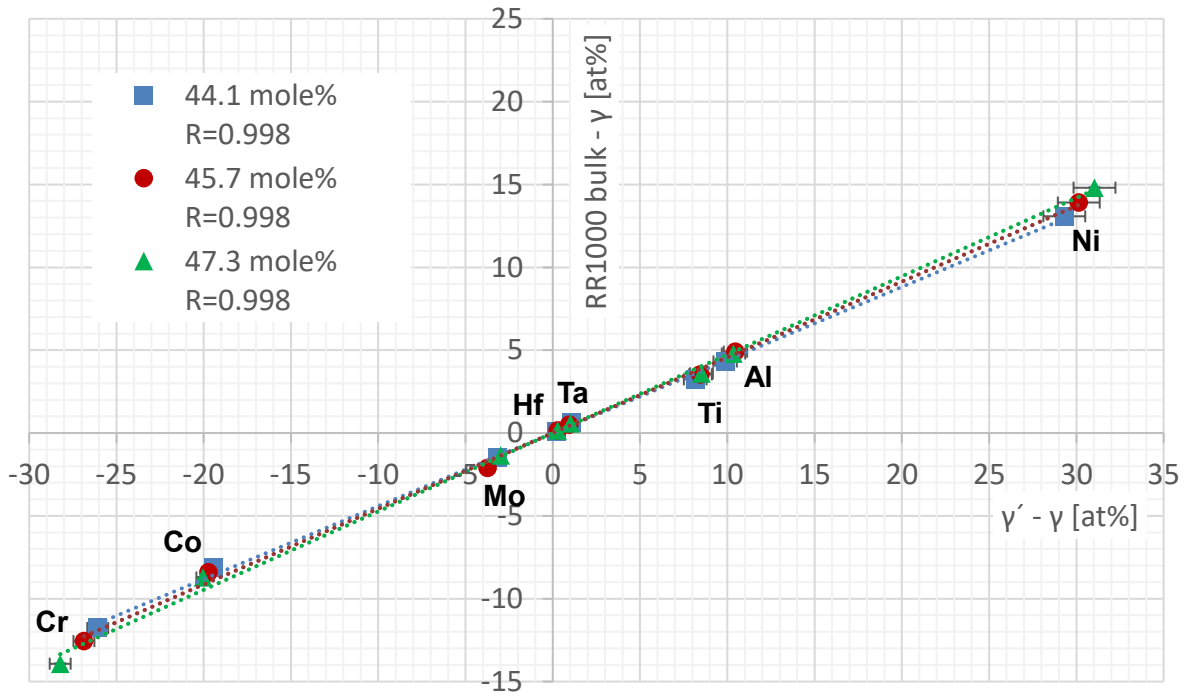

Figure 8 Lever rule diamgram of RR1000 aged at 750ºC for 150 hours with three sets of EDX data (based on three γ quantitative results); Square, circle and triangle data points show the smallest, intermediate and the largest γ´ mole fraction obtained, respectively. The error bars on the X axis were reffered from the standard deviations found in the γ´ analysis.

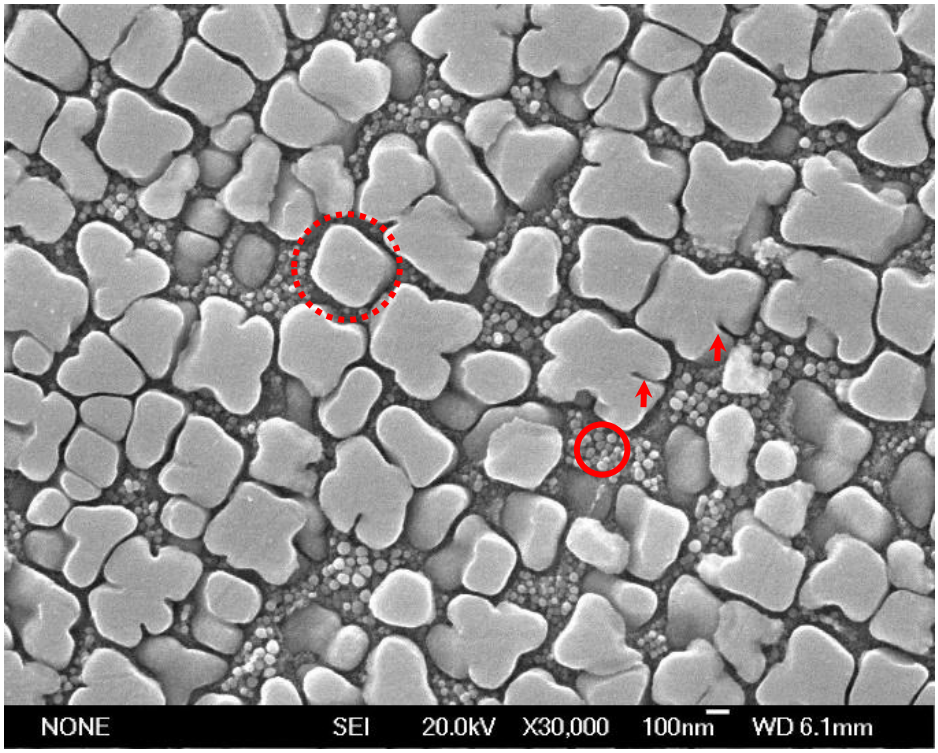

a)

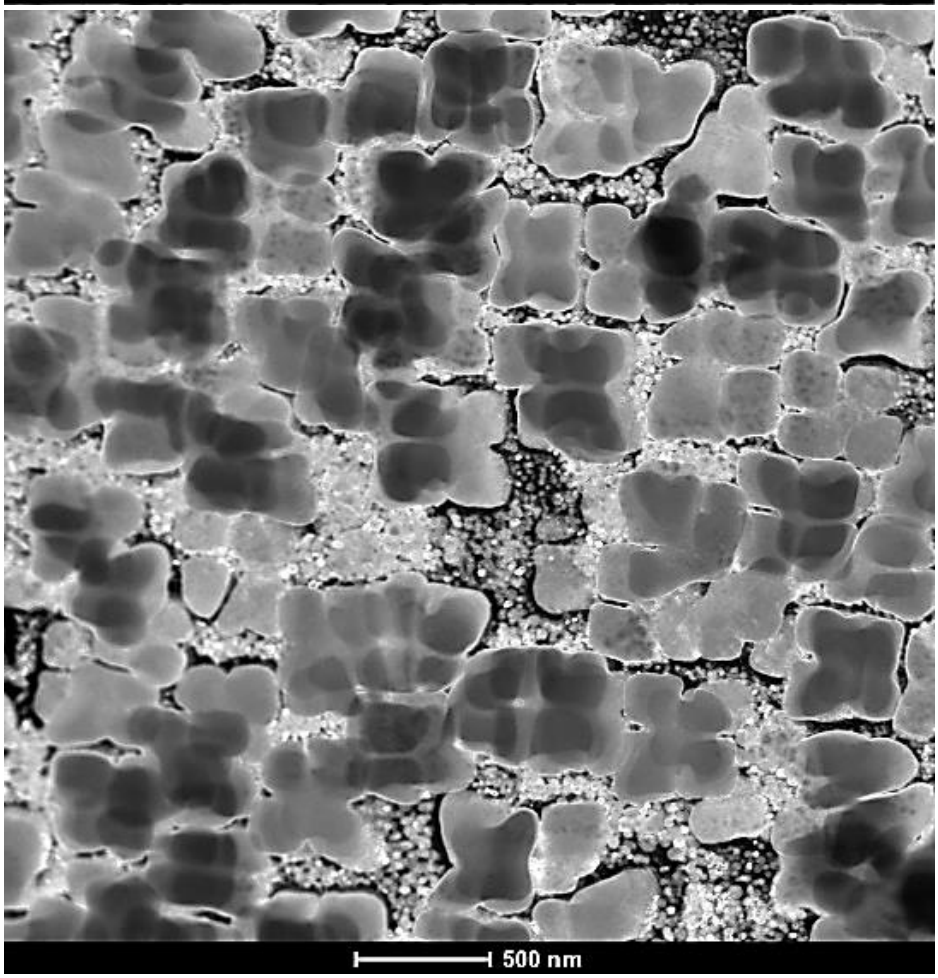

b)

Figure 9 Furnace cooled bimodal RRAlH micrographs:

(a) SEM secondary electron micrograph with coarse γ′ and fine γ′ indicated by broken and solid circles, respectively;

(b) STEM dark field micrograph after extraction replica.

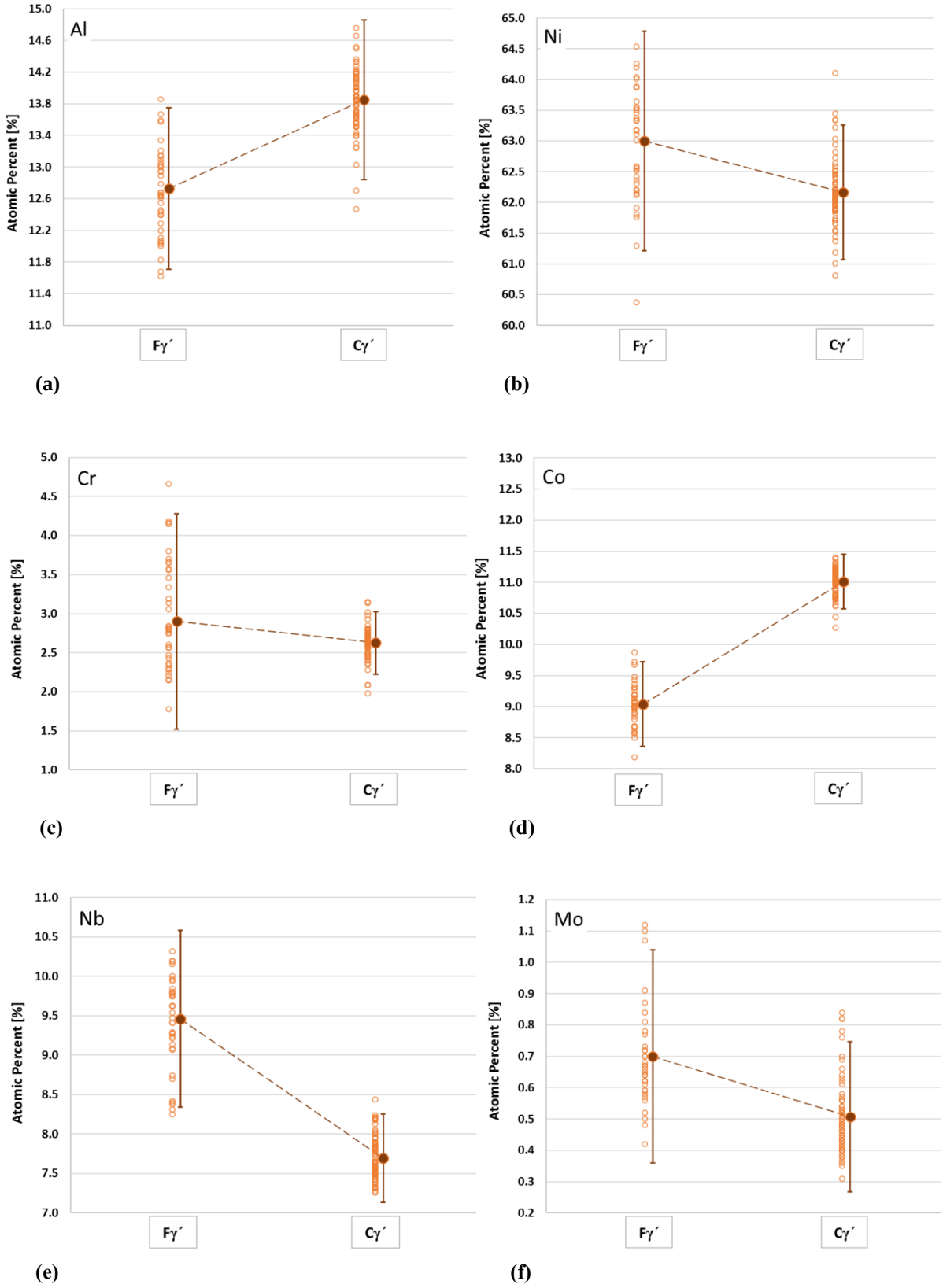

Figure 10 Summary of bimodal γ´ chemical analyses using the furnce cooled RRAlH. Fine γ´ and coarse γ´ are shown on the left and the right hand side of each diagram, respectively. In total, 38 fine γ´ and 58 coarse γ´ particles were measured and are plotted as open circles. The average and its 2σ standard deviation are shown via filled circles with an error bar for each generation of γ´.

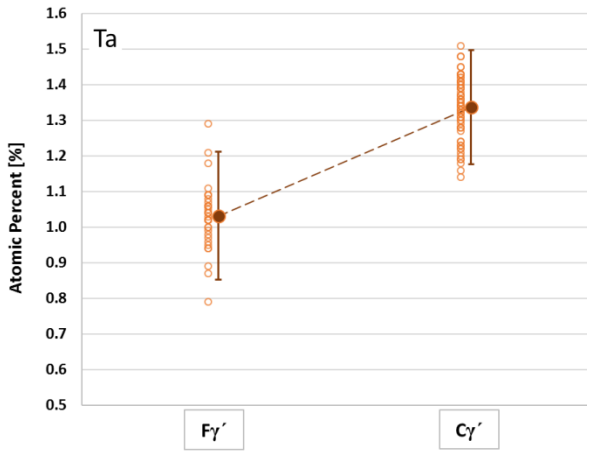

(g)

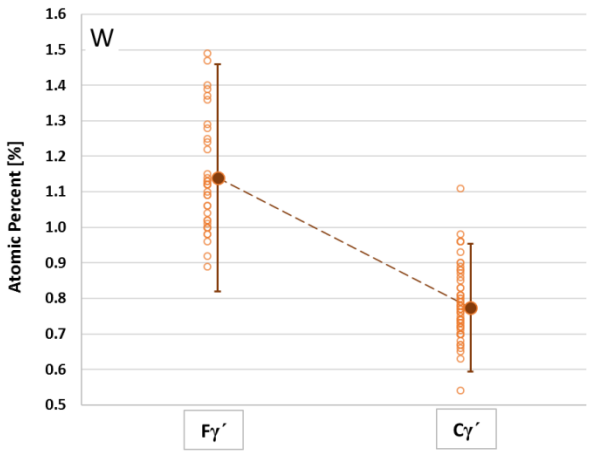

(h)

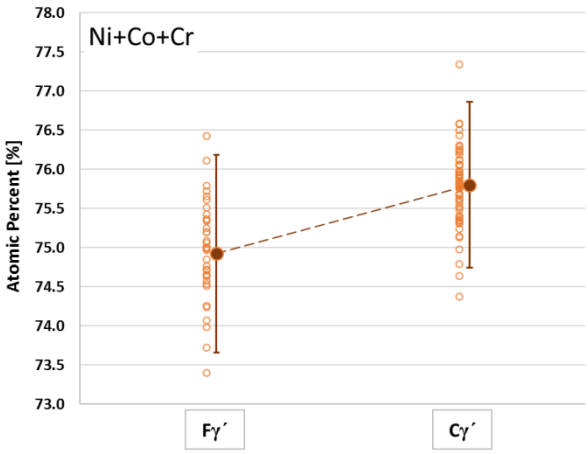

(i)

(j)

Figure 10 (Continued)

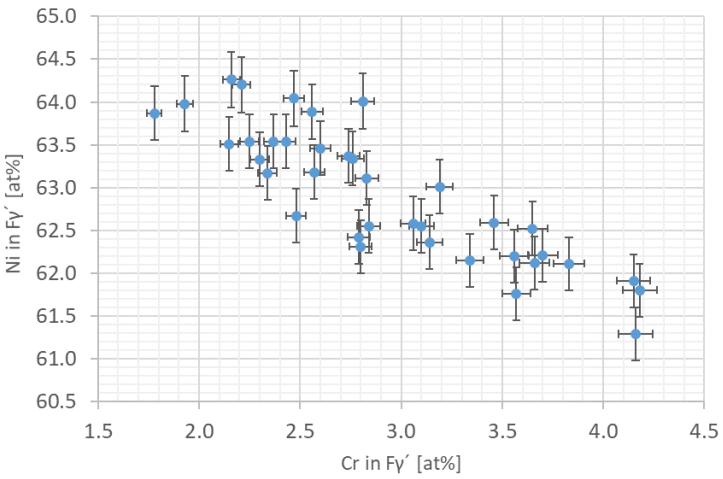

a)

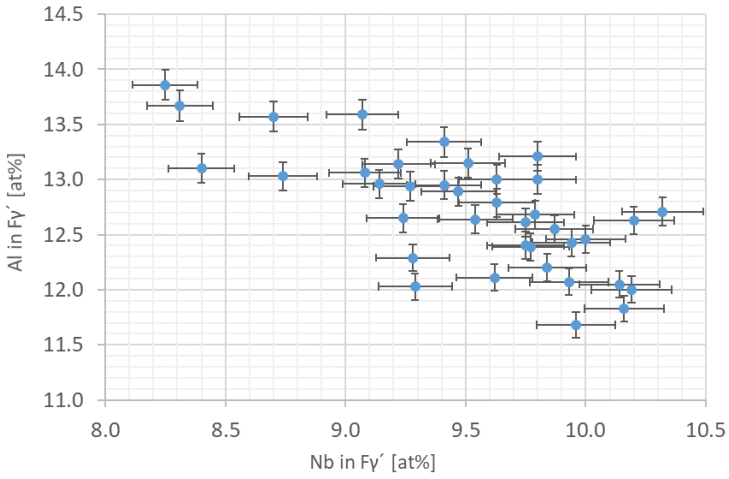

b)

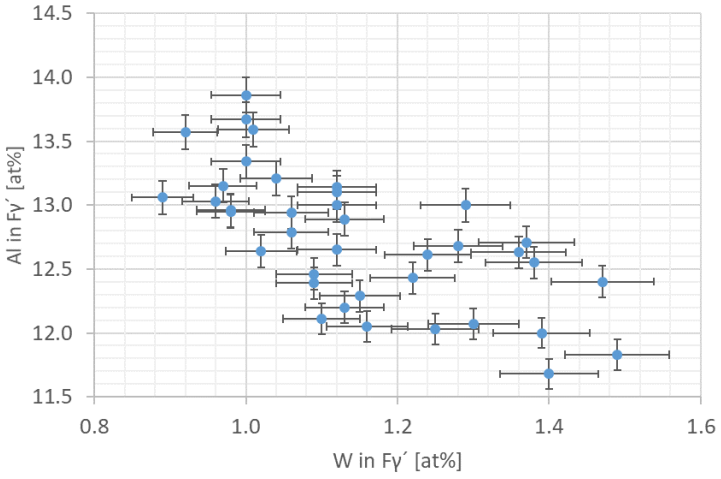

c)

Figure 11 Relationship between constituent elements of RRAlH for individual Fγ´ particles after furnace cooling and subsequent ageing at 850ºC for 4 hours

- **(a) Ni versus Cr**
- **(b) Al versus Nb**
- **(c) Al versus W**

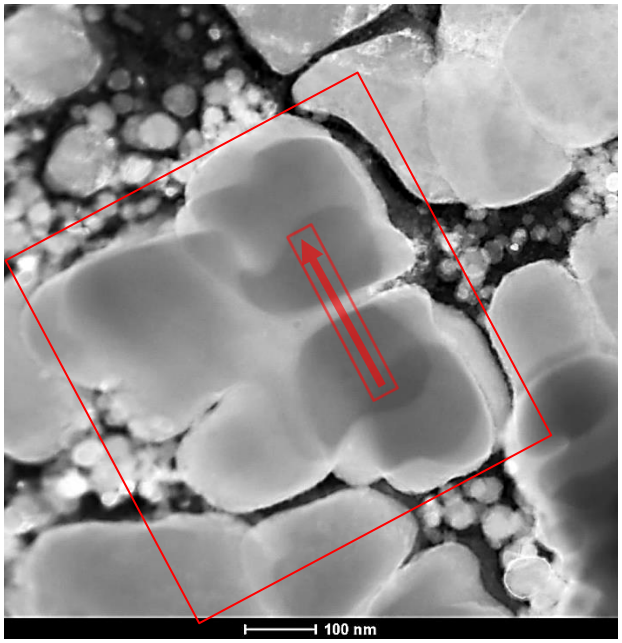

a)

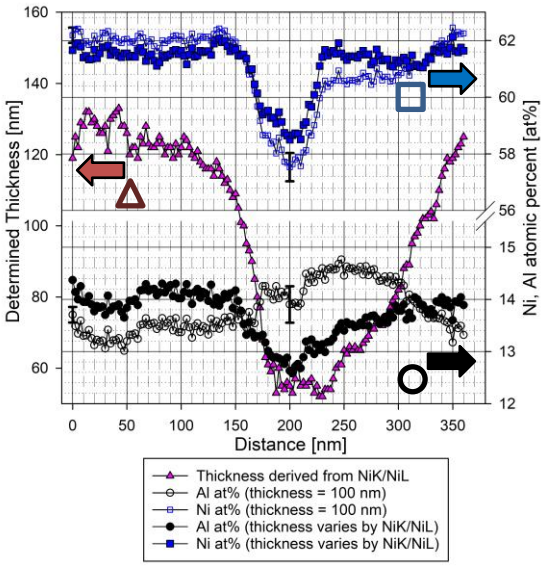

b)

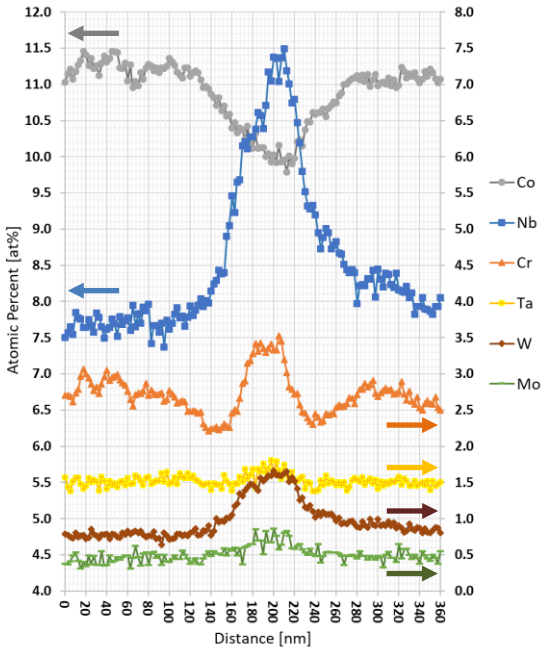

c)

Figure 12 STEM dark field micrograph of a heterogeneously evolved Cγ´ and chemical concentration profiles:

- **(a) STEM Dark field micrograph of the Cγ´ with an indication of the area and the direction of the EDX scan and the sample thickness determination;**
- **(b) Specimen thickness profiles using NiKα/NiLα ratios (triangles) and EDX concentration profiles of Al and Ni assuming a uniform sample thickness of 100 nm (open circles and squares) to demonstrate the difference from the results by the application of the various sample thicknesses determined by the NiKα/NiLα ratios (filled circles and squares);**
- **(c) EDX concentration profiles other than Al and Ni using the varied thicknesses across via the NiK/NiL ratios.**

References

[1] C.T. Sims, W.C. Hagel, The superalloys, Wiley-Interscience, 1972
[2] R.C. Reed, in, Cambridge University Press, 2006,
[3] J.S. Van Sluytman, A. La Fontaine, J.M. Cairney, T.M. Pollock, Acta Materialia, 58 (2010) 1952-1962.10.1016/j.actamat.2009.11.038
[4] H.Y. Li, J.F. Sun, M.C. Hardy, H.E. Evans, S.J. Williams, T.J.A. Doel, P. Bowen, Acta Materialia, 90 (2015) 355-369.10.1016/j.actamat.2015.02.023
[5] P.A.J. Bagot, O.B.W. Silk, J.O. Douglas, S. Pedrazzini, D.J. Crudden, T.L. Martin, M.C. Hardy, M.P. Moody, R.C. Reed, Acta Materialia, 125 (2017) 156-165.10.1016/j.actamat.2016.11.053
[6] J.S. Tiley, O. Senkov, G. Viswanathan, S. Nag, J. Hwang, R. Banerjee, Metallurgical and Materials Transactions A, 44 (2013) 31-38.10.1007/s11661-012-1456-2
[7] S.C.H. Llewelyn, K.A. Christofidou, V.J. Araullo-Peters, N.G. Jones, M.C. Hardy, E.A. Marquis, H.J. Stone, Acta Materialia, 131 (2017) 296-304.10.1016/j.actamat.2017.03.067
[8] Y. Amouyal, M. Zugang, D.N. Seidman, Acta Materialia, 58 (2010) 5898-5911.10.1016/j.actamat.2010.07.004
[9] W. Sha, L. Chang, G.D.W. Smith, L. Cheng, E.J. Mittemeijer, Surface Science, 266 (1992) 416-423.10.1016/0039-6028(92)91055-g
[10] H.S. Kitaguchi, S. Lozano-Perez, M.P. Moody, Ultramicroscopy, 147 (2014) 51-60.10.1016/j.ultramic.2014.06.004
[11] F. Vurpillot, A. Bostel, D. Blavette, Applied Physics Letters, 76 (2000) 3127-3129.10.1063/1.126545
[12] F. De Geuser, W. Lefebvre, F. Danoix, F. Vurpillot, B. Forbord, D. Blavette, in, John Wiley and Sons Ltd, 2007, pp. 268-272.10.1002/sia.2489
[13] Y.Q. Chen, T.J.A. Slater, E.A. Lewis, E.M. Francis, M.G. Burke, M. Preuss, S.J. Haigh, Ultramicroscopy, 144 (2014) 1-8.10.1016/j.ultramic.2014.04.001
[14] W. Mangen, E. Nembach, H. Schaefer, Materials science and engineering, 70 (1985) 205-210.10.1016/0025-5416(85)90282-4
[15] D. Mukherji, R. Muller, R. Gilles, P. Strunz, J. Rosler, G. Kostorz, Nanotechnology, 15 (2004) 648-657.10.1088/0957-4484/15/5/042
[16] A.J. Goodfellow, E.I. Galindo-Nava, K.A. Christofidou, N.G. Jones, T. Martin, P.A.J. Bagot, C.D. Boyer, M.C. Hardy, H.J. Stone, Metallurgical and Materials Transactions A, 49 (2018) 718-728.10.1007/s11661-017-4336-y
[17] Y.Q. Chen, E. Francis, J. Robson, M. Preuss, S.J. Haigh, Acta Materialia, 85 (2014) 199-206.10.1016/j.actamat.2014.11.009
[18] F.H. Harf, Journal of Materials Science Letters, 9 (1990) 78.10.1007/bf00722876
[19] E. Smith, J. Nutting, British Journal of Applied Physics, 7 (1956) 214-217.10.1088/0508-3443/7/6/304
[20] R.J. Mitchell, M.C. Hardy, M. Preuss, S. Tin, in: Superalloys 2004. Proceedings of the Tenth International Symposium on Superalloys sponsored by the TMS Seven Springs International Symposium Committee, in Cooperation with the TMS High Temperature Alloys Committee and ASM International, 19-23 Sept. 2004, TMS, Warrendale, PA, USA, 2004, pp. 361-370.10.7449/2004/Superalloys_2004_361_370
[21] H. Kitaguchi, Inertia Friction Welded RR1000 and Inconel718 Microstructure, University of Birmingham, School of Metallurgy and Materials, College of Engineering and Physical Sciences, 2010
[22] J.I. Goldstein, J.L. Costley, G.W. Lorimer, S.J.B. Reed, in: 10th Annual Scanning Electron Microscopy Symposium, 28 March-1 April 1977, IIT Res. Inst., Chicago, IL, USA, 1977, pp. 315-324
[23] M. Watanabe, D.B. Williams, Journal of Microscopy, 221 (2006) 89-109.10.1111/j.1365-2818.2006.01549.x
[24] Z. Horita, T. Sano, M. Nemoto, Ultramicroscopy, 35 (1991) 27-36.10.1016/0304-3991(91)90041-4
[25] M. Watanabe, Z. Horita, M. Nemoto, Ultramicroscopy, 65 (1996) 187-198
[26] Z. Horita, T. Sano, M. Nemoto, Ultramicroscopy, 21 (1987) 271-276.10.1016/0304-3991(87)90152-5
[27] Z. Horita, K. Ichitani, T. Sano, M. Nemoto, Philosophical Magazine A (Physics of Condensed Matter, Defects and Mechanical Properties), 59 (1989) 939-952.10.1080/01418618908209829

[28] M. Watanabe, Z. Horita, D.J. Smith, M.R. McCartney, T. Sano, M. Nemoto, Acta Metallurgica et Materialia, 42 (1994) 3381-3387.10.1016/0956-7151(94)90470-7
[29] R.F. Egerton, in: Electron-Beam-Induced Spectroscopies with High Spatial Resolution. NSF/CNRS Workshop, 28 Feb.-5 March 1988, Netherlands, 1989, pp. 215-225.10.1016/0304-3991(89)90299-4
[30] P.M. Kelly, A. Jostsons, R.G. Blake, J.G. Napier, Physica Status Solidi A, 31 (1975) 771-780.10.1002/pssa.2210310251
[31] S.M. Allen, Philosophical Magazine A (Physics of Condensed Matter, Defects and Mechanical Properties), 43 (1981) 325-335.10.1080/01418618108239412
[32] P.L. Morris, M.D. Ball, P.J. Statham, in: Electron Microscopy and Analysis, 1979, 3-6 Sept. 1979, Inst. Phys., Bristol, UK, 1980, pp. 413-416
[33] N. Ni, S. Lozano-Perez, J. Sykes, C. Grovenor, Ultramicroscopy, 111 (2011) 123-130.10.1016/j.ultramic.2010.10.020
[34] J. Tiley, G.B. Viswanathan, J.Y. Hwang, A. Shiveley, R. Banerjee, Materials Science and Engineering: A, 528 (2010) 32-36.https://doi.org/10.1016/j.msea.2010.07.036
[35] David B. Williams and C. Barry Carter, Transmission electron microscopy, 1996
[36] K. Aoki, O. Izumi, Physica Status Solidi (A) Applied Research, 32 (1975) 657-664
[37] X. Llovet, P.T. Pinard, E. Heikinheimo, S. Louhenkilpi, S. Richter, Microscopy and Microanalysis, 22 (2016) 1233-1243.10.1017/s1431927616011831
[38] X. Llovet, E. Heikinheimo, A.N. Galindo, C. Merlet, J.F.A. Bello, S. Richter, J. Fournelle, C.J.G.v. Hoek, IOP Conference Series: Materials Science and Engineering, 32 (2012) 012014
[39] F. Michel, X-Ray Spectrometry, 19 (1990) 169-172.doi:10.1002/xrs.1300190404
[40] B.L. Henke, E.M. Gullikson, J.C. Davis, Atomic Data and Nuclear Data Tables, 54 (1993) 181-342.https://doi.org/10.1006/adnd.1993.1013
[41] K.F.J. Heinrich, Proc. 11th Int. Congr. on X-Ray Optics and Microanalysis, (1986) 67-119
[42] J.-L. Pouchou, in: D. Benoit, J.-F. Bresse, L. Van't dack, H. Werner, J. Wernisch (Eds.) Microbeam and Nanobeam Analysis, Springer Vienna, Vienna, 1996, pp. 39-60
[43] D.M. Collins, L. Yan, E.A. Marquis, L.D. Connor, J.J. Ciardiello, A.D. Evans, H.J. Stone, Acta Materialia, 61 (2013) 7791-7804.10.1016/j.actamat.2013.09.018
[44] C. Yiqiang, R. Prasath babu, T.J.A. Slater, M. Bai, R. Mitchell, O. Ciuca, M. Preuss, S.J. Haigh, Acta Materialia, 110 (2016) 295-305.10.1016/j.actamat.2016.02.067
[45] A.R.P. Singh, S. Nag, J.Y. Hwang, G.B. Viswanathan, J. Tiley, R. Srinivasan, H.L. Fraser, R. Banerjee, Materials Characterization, 62 (2011) 878-886.https://doi.org/10.1016/j.matchar.2011.06.002
[46] K. Lohnert, F. Pyczak, in: 7th International Symposium on Superalloy 718 and Derivatives 2010, October 10, 2010 - October 13, 2010, John Wiley and Sons Inc, Pittsburgh, PA, United states, 2010, pp. 877-891
[47] S.T. Wlodek, M. Kelly, D.A. Alden, in: Proceedings of Eighth International Symposium on Superalloys, 22-26 Sept. 1996, TMS, Warrendale, PA, USA, 1996, pp. 129-136.10.7449/1996/Superalloys_1996_129_136
[48] B.S. Bokstein, S.Z. Bokstein, I.T. Spitsberg, Intermetallics, 4 (1996) 517-523.10.1016/0966-9795(96)00038-6
[49] C.E. Campbell, W.J. Boettinger, U.R. Kattner, Acta Materialia, 50 (2002) 775-792.10.1016/s1359-6454(01)00383-4
[50] J. Cermak, A. Gazda, V. Rothova, Intermetallics, 11 (2003) 939-946.10.1016/s0966-9795(03)00118-3
[51] J. Cermak, V. Rothova, Acta Materialia, 51 (2003) 4411-4421.10.1016/s1359-6454(03)00276-3
[52] L. Shaohua, L. Chengpeng, G. Lin, Z. Xiaona, Y. Tao, Y. Ping, W. Chongyu, Scripta Materialia, 138 (2017) 100-104.10.1016/j.scriptamat.2017.05.036
[53] M. McCormack, A.G. Khachaturyan, J.W. Morris, Acta Metallurgica et Materialia, 40 (1992) 325-336.https://doi.org/10.1016/0956-7151(92)90306-Y
[54] D. Banerjee, R. Banerjee, Y. Wang, Scripta Materialia, 41 (1999) 1023-1030.https://doi.org/10.1016/S1359-6462(99)00223-7
[55] S.V. Divinski, S. Frank, U. Sodervall, C. Herzig, Acta Materialia, 46 (1998) 4369-4380.10.1016/s1359-6454(98)00109-8